Spring 2013

Covalent attachment of a diimine tricarbonyl re(I) catalyst on solid state nano-material surfaces for solar carbon dioxide reduction

He He
University of New Hampshire, Durham

Recommended Citation

He, He, "Covalent attachment of a diimine tricarbonyl re(I) catalyst on solid state nano-material surfaces for solar carbon dioxide reduction" (2013). *Master's Theses and Capstones*. 790.
https://scholars.unh.edu/thesis/790

COVALENT ATTACHMENT OF A DIIMINE TRICARBONYL Re(I)

CATALYST ON SOLID STATE NANO-MATERIAL SURFACES FOR

SOLAR CO$_2$ REDUCTION

BY

HE HE

B.S. Anhui University, China, 2000

THESIS

Submitted to the University of New Hampshire

in Partial Fulfillment of the Requirement for the Degree of

Master of Science

In

Chemistry

May, 2013

UMI Number: 1523795

UMI

Dissertation Publishing

UMI 1523795

ProQuest

This thesis has been examined and approved.

_____

Thesis Director

Dr. Gonghu Li

Assistant Professor of Chemistry

_____

Dr. Roy P. Planalp

Associate Professor of Chemistry

_____

Dr. P. T. Vasudevan

Professor of Chemical Engineering

April 27, 2013

Date

ACKNOWLEDGEMENTS

First, I would like to express my sincerest gratitude to my advisor, Dr. Gonghu Li, for his support, encouragement as well as guidance during my graduate study in UNH. His insightful views and intelligent ideas contributed to my research and this thesis. It has been an honor to work with him in the past years. Second, I would like to thank Dr. Roy Planalp, for his inorganic classes and inspiring discussion in my research work. He also has a valuable advice on this thesis writing. I would also like to thank Dr. Vasudevan, for his support and for being part of my graduate committee.

Dr. Ed Wong, Dr. Sterling Tomellini and Dr. Rudolf Seitz, thanks for your enthusiasm and patience in teaching classes, and also thanks for the other supports during my academic career. All the other professors and staffs in Chemistry department are also appreciated. Thanks for the help from Cindi Rohwer, Peggy Torch, Amy Lindsay and Bob Constantine.

My lab colleagues, Kevin Dubois, Tong Jin, Chao Liu and Mike Louis, thanks for your support in both my research and my daily life. It's a great pleasure to work with you and it will be a great memory in my life.

Last but not least, I would like to thank my family, for their endless love in my whole life.

TABLE OF CONTENTS

LIST OF FIGURES

LIST OF SCHEMES

LIST OF TABLES

ABSTRACT

COVALENT ATTACHMENT OF A DIIMINE TRICARBONYL Re(I) CATALYST ON SOLID STATE NANO-MATERIAL SURFACES FOR SOLAR CO$_2$ REDUCTION

By

He He

University of New Hampshire, May, 2013

Reduction of carbon dioxide to useful chemicals and fuels is of significant interest. Transition metal complexes, such as tricarbonyl rhenium(I) compounds, are efficient molecular catalysts for photocatalytic carbon dioxide reduction. To improve the stability and catalytic activity of homogeneous catalysts, a mesoporous silica material, SBA-15, was synthesized and applied as catalyst support for immobilizing the tricarbonyl rhenium(I) compound via both covalent bonding and physical adsorption. The covalently bonded tricarbonyl rhenium(I) catalyst in SBA-15 exhibited excellent stability and good activity during the

photocatalytic reduction process, compared with its homogeneous counterpart and the physically absorbed one. Another solid-state nano-material, Kaolin, was also employed as a catalyst support for the covalent attachment of tricarbonyl rhenium(I) compound. The surface functionalized Kaolin displayed some new features in infrared studies due to the unique layered structure of Kaolin materials. These new features were further investigated with FTIR spectroscopy in the presence of a sacrificial electron donor. The synthesis and characterization of different microporous and mesoporous materials are also discussed.

CHAPTER 1

INTRODUCTION

1.1 Transition metal complexes as molecular catalysts for solar CO_2 reduction

With the continued industrialization and on-going growth of human population, energy consumption has been one of the most vital topics of the 21st century. According to the International Energy Agency, the average energy use per person from 1990 to 2008 increased 10% while during that period the world population increased 27%. The primary energy sources are still fossil fuels such as petroleum, natural gas and coal. As a result of the combustion of fossil fuels, the emission of carbon dioxide has continued to rise in the past decades. This increasing of atmospheric carbon dioxide results in global warming and climate change, which significantly affect human beings' living environment and the economic development. Governments, environmental protection organizations as well as scientists are devoted to looking for various methods to decrease the carbon dioxide content in the atmosphere. Besides all the efforts to cut down CO_2 emission, one idea is utilizing CO_2, the abundant carbon source as a feedstock to synthesize useful chemicals or fuels such as CO, carboxylic acids, esters, methane, methanol and polymers. This is not only a way to reduce the

atmospheric CO_2 concentration, but also a solution for the energy crisis we are facing.

Although utilization of CO_2 has a very brilliant future, the actual transformation procedure is full of challenges and obstacles.[1] For example, at the highest oxidation state of carbon cycle, CO_2 is extremely stable with a very high C=O bond energy of 799 kJ/mol. It is very hard to break the C=O double bond or active the molecule either electrochemically or thermochemically. As a result, a huge amount of energy needs to be put into the reactions in the converting systems.[2] Table 1.1 shows the energy barriers of reactions involving CO_2 conversion.

Table 1.1 CO_2 Reduction Potentials[2]

Reaction	E° (V) vs. SCE*
$CO_2 + 2H^+ + 2e^- \rightarrow HCO_2H$	-0.85
$CO_2 + 2H^+ + 2e^- \rightarrow H_2O + CO$	-0.77
$CO_2 + 4H^+ + 4e^- \rightarrow 2H_2O + C$	-0.44
$CO_2 + 4H^+ + 4e^- \rightarrow H_2O + HCHO$	-0.72
$CO_2 + 6H^+ + 6e^- \rightarrow H_2O + CH_3OH$	-0.62
$CO_2 + 8H^+ + 8e^- \rightarrow 2H_2O + CH_4$	-0.48

* E° potentials are reported at pH 7

The history of scientific studies on CO_2 utilization can be traced back decades, but most of the methods are still cost prohibitive and have a long distance to practical applications. One way to reduce the cost is using a renewable energy source such as solar energy as input energy. Although solar energy has some

drawbacks such as regional limitation, seasonal availability and energy density issues, the benefits are still attractive because it is free, clean and will never dry up. To utilize solar energy for CO_2 reduction, having a catalyst with photoresponse to solar light irradiation is a vital factor in the system, because photo-excited catalysts can undergo a charge separation process and transfer electrons in the reaction system. Accordingly, high oxidation state CO_2 could be reduced to its lower oxidation states upon accepting of electrons. So the primary goal of our research is to develop highly efficient photocatalysts to absorb solar energy and lower the energy barriers of the CO_2 reduction reactions.

In nature, metal complexes as enzymes or co-enzymes play an important role in biological processes. Chlorophylls, which include a family of magnesium porphyrin complexes, are extremely important in green plants photosynthesis. Coordination of inert molecules with metal complexes is an effective approach to activating chemically stable substances in order to produce desired reactions. Using transition metal coordination compounds as homogeneous catalysts for CO_2 reduction has been intensively studied in the last 30 years.[3,4,5,6] CO_2 is a linear molecule with two equivalent carbon-oxygen double bonds. By exciting the molecule to its lowest excited state or by attracting from electron donors, the CO_2 molecule's configuration will be changed from linear to non-linear, thus we could expect CO_2 molecule to display multiple coordination modes with transition metal complexes[7]: (I) metal donates electrons to the carbon orbital forms a metallo-acid derivative; (II) formation of a π-complex via C=O double bond and (III) an oxygen atom in CO_2 donates a lone pair of electrons to the empty orbital of metal (Figure

3

1.1). Because CO_2 molecules are poor electron donors but good electron

acceptors, type I and II are the most common ways of CO_2 molecules coordinate

with metal complexes while the third type is less likely.

(I)   (II)   (III)
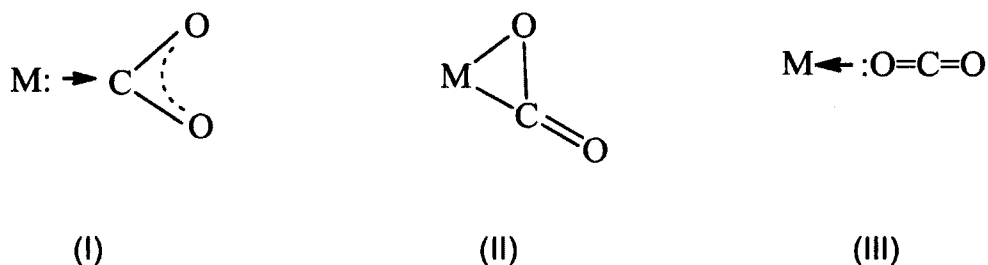
Figure 1.1 Three coordination types for CO_2 on a metal center

Up to now, reported transition metal complexes that have CO_2 reduction activity

include cobalt, nickel, rhenium, rhodium, platinum, iridium and ruthenium

complexes. Based on their composition, these metal coordination compounds

are usually grouped as: metal tetraaza-macrocyclic complexes; supramolecular

complexes; metalloporphyrins and related metallomacrocycles and

$Re(CO)_3(bpy)X$-based compounds where bpy is 2,2'-bipyridine and X is Cl⁻. [2]
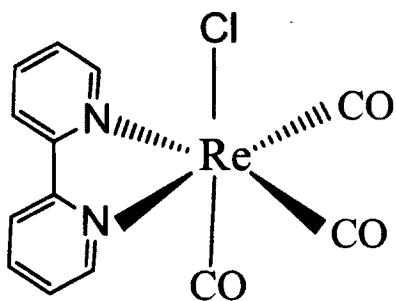
Figure 1.2 Structure of a *fac*-Re(CO)₃(bpy)Cl, where bpy=2,2'-bipyridine

In 1983, Hawecker and co-workers firstly reported a $Re^I(L)(CO)_3X$ compound (Figure 1.2), where L= 4,4'-R_2-2,2'-bipyridine (R= H or CH_3) and X=Cl^- or Br^-, as a photochemical CO_2 reduction catalyst.[8] Since then tricarbonyl rhenium(I) based catalysts have been intensively studied. Among all the CO_2 reduction catalysts that have been investigated, $Re^I(L)(CO)_3X$ exhibits the best reaction selectivity to produce CO and a high photochemical quantum yield, although the turnover number is relatively low due to the decomposition of the complex upon photo irradiation (the best reported value is 48 by Hawecker and co-workers[8]). The UV-Vis spectra indicate $Re^I(L)(CO)_3X$ complexes can only absorb light with wavelengths under 380nm. To improve the absorption of visible light in the catalytic reaction, additional photosensitizers, usually polypyridyl ruthenium complexes, are added to the reaction system.[2,9] The advantage of polypyridyl ruthenium complexes as photosensitizer is $Ru(bpy)_3^{2+}$ can absorb significant amount of visible light in a wide range and form an excited triplet state (^{3}MLCT), which has much longer life time than the singlet excited state (^{1}MLCT) of other metal complexes.[10] The long-lived excited state of Ru complexes enables the effective charge separation in the reduction system.

In the last 20 years, homogeneous photocatalytic CO_2 reduction studies have greatly progressed. Ishitani and co-workers developed various homogeneous catalysts systems to improve the reactions activity.[4,9,11] However, the stability and quantum efficiency of currently available photocatalysts are still low. Moreover, most of the catalysts are very expensive transition metal compounds.

Improving the catalyst stability under photocatalytic reaction condition is another

challenge for us.

1.2 Nanoporous materials as molecular catalyst supports

Nano-materials are fascinating because at this small size scale, atoms

and molecules interact and arrange in certain patterns, exhibiting unique

properties that bulky materials do not have. Nanoporous material is one

important subset of nano-materials that render a lot of superior properties due to

high surface areas, ordered pore structures and uniform pore size. According to

the definition of International Union of Pure and Applied Chemistry (IUPAC),

porous materials are usually divided into three classes: (1) micropores are pore

sizes less than 2 nm in diameter; (2) mesopores are pore diameters between 2

and 50 nm and (3) macropores are pore diameters greater than 50 nm.[12,13]

Functional nanoporous materials usually have pore sizes between 1 to 100 nm

and typically have porosities greater than 0.4 (porosity is the ratio of pore volume

to the total volume of material). According to the materials chemical composition

(organic or inorganic; metal or ceramic), their properties vary as well.

Nanoporous materials have various applications like separation, sensing,

chromatography as well as catalysis. In this thesis, nanoporous zeolites and

silica materials have been studied because besides the high surface areas and

ordered porous structures, they are also non-toxic, chemically inert and thermally

stable, which make them the ideal candidates as catalysts or catalyst supports for our photocatalytic study.

1.2.1 Microporous zeolites (molecular sieves)

Zeolites are crystalline, microporous aluminosilicates, constituted of tetrahedral SiO_4 and AlO_4 building blocks. Because of their molecular level porous structures they are also known as "molecular sieves". According to the database of the Structural Commission of the International Zeolite Association (IZA-SC), 206 unique types of zeolites frameworks have been identified up to now and the most common types such as ZSM-5, Na-Y and Silicalite-1 have been synthesized and their surface areas and pore sizes are adjustable by manipulating synthesis conditions.[14,15,16] Figure 1.3 shows the crystal structures of ZSM-5 and Na-Y.

(a)   (b)
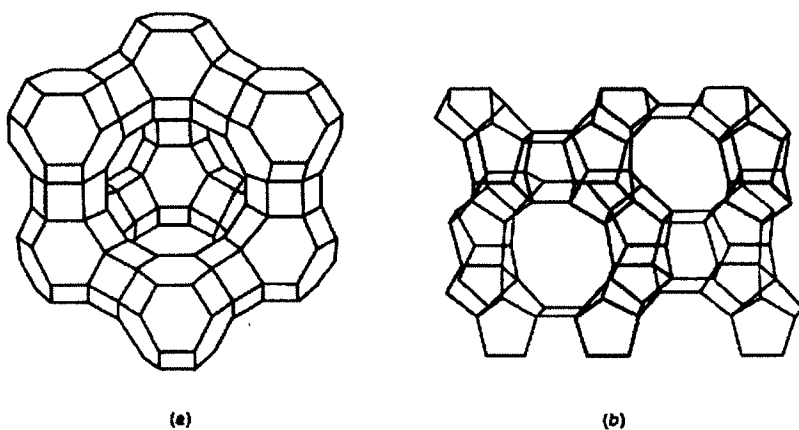
Figure 1.3 Illustrations of the structures of (a) NaY and (b) ZSM-5[17]

As mentioned before, zeolites are composed of tetrahedral silicon-oxygen and tetrahedral aluminum-oxygen units. SiO_4 units are electrically neutral since the Si exits in a 4+ oxidation state; however, AlO_4 tetrahedra exhibit a negative charge because the Al exits in a +3 oxidation state. So in general, zeolite frameworks are electronic deficient and additional cations are often needed by the structures to compensate the positive charge deficiency to form charge-neutral frameworks. When these charge compensating cations are involved in ion-exchange processes, zeolites will exhibit some important properties for functional applications. For example, when protons as compensating cations adopted by the frameworks, zeolites exits as strong solid-acids. This property renders zeolites work as catalysts in various reactions.

1.2.2 Mesoporous silica

According to the IUPAC definition, mesoporous materials are materials with pore diameters between 2 and 50 nm.[13] Mesoporous silica is one of the most popular mesoporous materials, which have been tremendously developed in the last 20 years. The first procedure of mesoporous silica synthesis was invented in 1970s.[18] In 1990, Japanese scientists Yanagisawa et al. synthesized the mesoporous silica nanoparticles, which were also produced by Mobil Corporation laboratories and named as Mobil Crystalline Materials or M41S.[19] The hexagonally packed rod-shaped silica, MCM-41 is one of the best known and intensively studied nanostructured silica in the M41S family. Other types like MCM-48 with a cubic pore symmetry and lamellar MCM-50 are also included in the M41S family.

In 1998, Zhao et al. in University of California, Santa Barbara invented a new family of mesoporous silica named as Santa Barbara Amorphous.[20] The most famous member in this family, SBA-15, has an ordered 2-dimentional hexagonal arranged pore structure that is very similar to the structure of the MCM-41. Compare to MCM-41 silicas, SBA-15 silicas usually have thicker silica walls and larger pore sizes. Using tri-block copolymers such as Poly (ethylene glycol)-poly (propylene glycol)-poly (ethylene glycol) as structure templating agents can produce mesoporous silicas SBA-15 with average pore diameters between 50–300 Å. The pore walls of SBA-15 materials are remarkably thick (60–70 Å), with micro pores inside them, which are connecting with the mesoporous structures[20]. These features make the SBA-15 materials more physically robust and structurally stable than the MCM-41 silicas. In Figure 1.4, the SEM images indicate a representative SBA-15 material's particle size and morphology, while the TEM images reveal the pores' structure.[20] The excellent properties of mesoporous silica materials such as remarkably large surface areas (could be greater than $1000m^2/g$), ordered mesoporous constructions and highly chemical and thermal stability bring about extensive applications of these materials, such as sorption, drug delivery, chromatography, separation and catalysis[21]. Moreover, the existence of surface silanol groups in mesoporous silicas, which renders them be capable of surface modification, has also attracted a lot of interests from researchers. In this thesis, SBA-15 silicas with various morphology and pore sizes are synthesized and applied in our photocatalytic CO_2 reduction studies as a solid state catalyst support.

9
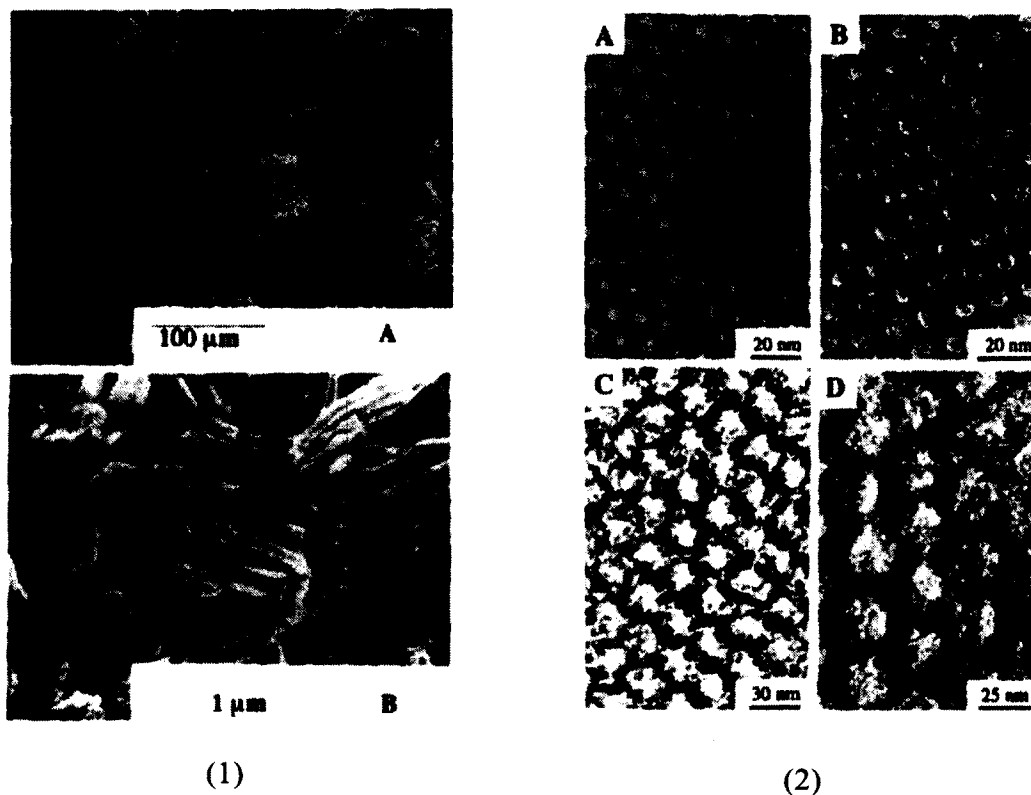
Figure 1.4 (1) SEM of a rod-shaped SBA-15 with uniform particle size around 1 μm; **(2)** TEM images of four calcined SBA-15 silicas with different average pore sizes: **(A)** 60 Å, **(B)** 89 Å, **(C)** 200 Å and **(D)** 260 Å.[20]

1.3 Advantages of surface immobilization of molecular catalysts

Catalysis is extremely important in a lot of chemical procedures; pursuing "ideal catalysts" is always one of the central missions of researchers. Scientists have tried different approaches to improving catalysts' quality in multiple aspects. As for homogeneous catalysis, modification of catalyst molecules by "tailoring" with functional groups or other molecules is a valid method to improve catalytic activity. For example, supramolecular complexes for photocatlytic CO_2 reduction

10

are prepared by tailoring another complex (usually a photosensitizer) with a catalyst complex by covalent linkage to achieve significant activity enhancement.[9] Another effective way is mixing two different catalysts to form a bimolecular catalysis system to improve the catalysts' performance.[22] However, modification of homogeneous catalysts is usually time consuming, costly, requiring strict reaction conditions and suitable reagents. In addition, the stability and lifetime of homogeneous catalysts are relatively low especially under harsh reaction conditions like high temperature, intense light irradiation or high acidity. For those very expensive catalysts, such as rhenium and ruthenium compounds, the question of how to improve these materials' stability and recyclability is a critical challenge to researchers.

Surface immobilization of homogeneous catalysts with robust solid-state materials is an effective and commonly utilized method to deal with the drawbacks of homogeneous catalysts. Surface immobilization is attachment of molecular catalysts onto the surfaces of solid-state supporting materials in order to achieve enhancement in stability and catalytic properties. The primary surface immobilization methods include physical adsorption and covalent binding, each of the methods has advantages and disadvantages in specific aspects. In general, physical adsorption is the simplest and most economical way of surface immobilization, enabling catalysts to settle on solid-state surfaces under mild conditions without any chemical changes to either the catalysts or the supporting materials. Accordingly, it is possible to retain catalytic activity and other properties of the catalysts. However, the drawbacks of this method are also

significant. For example, the interaction between catalyst molecules and support materials is very weak so catalysts tend to leak from the supports especially under harsh conditions like high ionic strength, high or low pH, strong light irradiation, etc. Moreover, because there is no specific bonding between catalysts and surfaces, it is hard to control catalysts' loading on surfaces. Consequently, another surface immobilization technique, covalent binding, was developed to solve the short comings of physical adsorption. This method involves covalent bonds forming between catalysts and supports via chemical reactions. As a result, catalyst molecules or their derivatives react with the surface functional groups such as surface hydroxyl groups to form covalent linkages between them, therefore, the catalysts are firmly attached on the surfaces through covalent bonds.

Although this technique has its own drawbacks such as the high cost, requiring strict reaction conditions and the possible loss of partial catalytic activity due to the chemical changes, it is still very attractive because of the superiority of the covalent bonding. With the strong covalent linkages, catalysts molecules are firmly fixed on the support surfaces, so there is no leakage of catalysts during reaction processes. The thermal and chemical stability of catalysts are improved as well, and moreover, material's recyclability becomes feasible.

In recent years, investigating heterogeneous catalysts for photocatalytic CO_2 reduction has led to a new research direction. By now, many heterogeneous catalysts for CO_2 reduction have been investigated; they exhibit a lot of advantages in reactions that homogeneous catalysts do not have. For examples,

12

TiO$_2$-based nanomaterials are robust and stable.[23] Surface-immobilized molecular catalysts have the merits of both homogeneous catalysis and heterogeneous catalysis.[24] Ishitani and co-workers have incorporated the Re(I) catalyst in an organic-inorganic hybrid periodic mesoporous organosilica to combine the advantages of the organic molecules and the ordered mesoporous structures.[25] This present study investigated surface immobilization of a tricarbonyl Re(I) catalyst on mesoporous silica SBA-15 surface via both physical adsorption and covalent bonding to pursuing enhanced stability and activity of the catalysts. The covalent bonded catalyst exhibited excellent performance in the photo CO$_2$ reduction reactions due to the improved stability and the derived functional group of the rhenium(I) catalyst molecule.

To further investigate how the supporting material's structures affect properties and performance of the catalysts in the photocatalytic CO$_2$ reduction process, a different structured nanomaterial, Kaolin was also employed in the surface immobilization with a tricarbonyl Re(I) complex for heterogeneous CO$_2$ reduction. Kaolin is a 1:1 dioctahedral aluminosilicate with layered crystalline structure. The chemical composition of kaolin is Al$_2$Si$_2$O$_5$(OH)$_4$,[26] which indicates the existence of abundant hydroxyl groups in Kaolin. With one tetrahedral siloxane face linked through oxygen atoms to one octahedral gibbsite (Al(OH)$_3$) sheet, the 1:1 layered structure is formed for Kaolin. The immobilization of a tricarbonyl Re(I) catalyst on Kaolin surface followed the same procedure as that for immobilization of Re (I) compound on silica SBA-15. The obtained Re(I)

catalyst immobilized on Kaolin exhibited some interesting new features in the IR

spectra.

CHAPTER 2

EXPERIMENTAL

2.1 Materials

Tetrapropylammonium hydroxide (TPAOH); Aluminum isopropyloxide; Tetraethyl orthosilicate (TEOS); ethanol; Poly(ethylene glycol)–poly(propylene glycol)–poly(ethylene glycol) (Pluronic P-123); Hexadecyltrimethylammonium bromide (CTAB); 2,2'-bipyridine-4,4'-dicarboxylic acid; thionyl chloride ($SOCl_2$); triethylamine (TEA); Triethanolamine (TEOA); 3-aminopropyltrimethoxysilane (APTMS); propylamine; pentacarbonyl chlororhenium(I); Acetonitrile and Dimethylformamide (DMF); Tris(2,2'-bipyridyl)dichlororuthenium(II) hexahydrate were all obtained from Sigma–Aldrich and used without further treatment.

2.2 Instrumentation

Scanning Electron Microscope (SEM) images were taken by an Amray 3300FE field emission SEM with PGT Imix-PC microanalysis system.

X-Ray Diffraction (XRD) patterns were obtained from a D/Max-2TB X-RAY DIFFRACTOMETER SYSTEM, Rigaku.

UV–visible spectra were obtained on a Cary 50 Bio spectrophotometer fitted with a Barrelino diffuse reflectance probe using $BaSO_4$ as a standard and powder samples pressed on $BaSO_4$ pellets.

Infrared spectra were collected on a Nicolet 6700 FTIR spectrometer equipped with a Harrick Praying Mantis diffuse reflectance accessory, a three-window chamber and a DTGS detector and a Nicolet iS10 FTIR spectrometer equipped with attenuated-total-reflectance (ATR) accessory.

Surface area, pore size distribution and total pore volume of the synthesized microporous zeolites and mesoporous SiO_2 were measured on a NOVA 2200e surface area and pore size analyzer.

Elemental analysis was conducted using a Costech ECS4010 Elemental Analyzer interfaced to a DeltaPlus mass spectrometer via a Conflo III and a Varian Vista AX induced coupled plasma atomic emission spectrometer.

Gas Chromatography was measured on an Agilent 7820 GC equipped with a TCD detector and a 60/80 Carboxen 1000 column.

2.3 Synthesis

Zeolite ZSM-5

To start the synthesis, 9 ml of 1 mol/L Tetrapropylammonium hydroxide aqueous solution, 6.4 mg sodium hydroxide, 204 mg Aluminum isopropyloxide, 5.2 g

Tetraethyl orthosilicate, 8.9 ml of deionized water and 5.8 ml ethanol were mixed as reaction gel, kept stirred for 12 hours at room temperature, then the clear solution was transferred into a Teflon lined autoclave and heated at 165°C for 120 hours. The autoclave was completely cooled down and centrifuged to recover the products. The products were washed with deionized water 5-6 times to get rid of the residual chemicals and dried at room temperature overnight. To remove the templates from the crystals, the dried products were calcined at 600°C for 6 hours with oxygen flow.

Zeolite Silicalite-1

The reaction gel was obtained by mixing 9 ml of 1 mol/L Tetrapropylammonium hydroxide aqueous solution, 6.4 mg sodium hydroxide, Tetraethyl orthosilicate, 8.9 ml of deionized water and 5.8 ml ethanol, stirred at room temperature for 12 hours then transferred the solution into a Teflon lined autoclave, kept it at 165°C for 120 hours. Then the products were recovered by centrifuge after the materials were cooled down. This was washed with deionized water 5-6 times and dried at room temperature overnight. Then the materials were calcined at 600°C for 6 hours with oxygen flow to remove the TPAOH templates in the particles.

SBA-15 Silicas

For batch #1, the synthesis was started by dissolving 1 g of Pluronic P-123 triblock copolymer in 37.5 ml of 1.6 M aqueous HCl solution with stirring until all the polymers are dissolved, followed by adding 2.1 g of TEOS drop wise with vigorous stirring. The resulting gel was stirred at room temperature for 12 hour, then transferred to a Teflon-lined autoclave and heated at 180°C for 16 hours. After cooling down to room temperature, the product was covered by filtration, washed with deionized water several times to get rid of residual chemicals and dried at 60°C overnight. To remove the copolymer templates, the dried product was calcined in tube furnace with flowing O_2 at 550°C for 6 hours.

The other batches of SBA-15 were produced by the same procedure as that for batch #1, but the composition of reaction gels and hydrothermal treatment temperature and time were varied (see table3.1).

Re-L-SiO$_2$

First, 52 mg of 2,2'-bipyridine-4,4'-dicarboxylic acid was refluxed under N_2 in 5 ml of $SOCl_2$ for 24 h and dried under vacuum to remove excess $SOCl_2$ and any generated amounts of HCl or SO_2. The resulting product, 4,4'-bis(chlorocarbonyl)-2,2'-bipyridine, was mixed with 0.12 ml of TEA and 0.074 ml of APTMS in 30 ml of chloroform and refluxed under N_2 for 1 h. A solution of the synthesized 4,4'-bis(3 trimethoxysilylpropyl)amido-2,2'-bipyridine in chloroform was mixed with 100 mg of SBA-15 SiO$_2$. The mixture was stirred for 2 days at

room temperature before the functionalized SiO$_2$ was filtered and washed with chloroform, methanol, and diethyl ether, and dried overnight at 40 °C to form SiO$_2$-L. In order to synthesize SiO$_2$-L-Re, 100 mg of SiO$_2$-L and 50 mg of pentacarbonyl chlororhenium(I) were dispensed in 40 ml of toluene and refluxed overnight. The final product was filtered, washed with toluene and dichloromethane, and dried overnight at 40 °C to yield a yellow powder.

Re + SiO$_2$

20 mg of the mesoporous SiO$_2$ was dispersed into a 40-ml solution of toluene containing 17 mg of Re-bpy and refluxed overnight. The product was filtered, washed with toluene and diethyl ether, and dried overnight at 40 °C to yield a slightly yellow powder, "SiO$_2$ + Re".

Re-L-Kaolin

52 mg of 2,2'-bipyridine-4,4'-dicarboxylic acid was refluxed under N$_2$ in 5 ml of SOCl$_2$ for 24 h and dried under vacuum to remove excess SOCl$_2$ and any generated amounts of HCl or SO$_2$. The resulting product, 4,4'-bis(chlorocarbonyl)-2,2'-bipyridine, was mixed with 0.12 ml of TEA and 0.074 ml of APTMS in 30 ml of chloroform and refluxed under N$_2$ for 1 h. A solution of the synthesized 4,4'-bis(3 trimethoxysilylpropyl)amido-2,2'-bipyridine in chloroform was mixed with 100 mg of Kaolin. The mixture was stirred for 2 days at room

temperature before the functionalized Kaolin was filtered and washed with chloroform, methanol, and diethyl ether, and dried overnight at 40 °C to form Kaolin-L. In order to synthesize Re-L-Kaolin, 100 mg of Kaolin-L and 50 mg of pentacarbonyl chlororhenium(I) were dispensed in 40 ml of toluene and refluxed overnight. The final product was filtered, washed with toluene and dichloromethane, and dried overnight at 40 °C to yield a yellow powder, Re-L-Kaolin.

2.4 Photocatalytic CO_2 reduction test

Surface functionalized SBA-15 Silicas

When comparing SiO_2-L-Re with SiO_2 + Re in photocatalysis, 10 mg of surface functionalized SiO_2 were dispersed in a Pyrex test tube containing a 5-ml mixture of acetonitrile and TEA (4:1 acetonitrile-to-TEA volume ratio). Because of the low solubility of Re-L in acetonitrile, dimethylformamide was used as the solvent for comparison between SiO_2-L-Re and Re-L, in which10 mg of SiO_2-L-Re or 3.2 mg Re-L were dispersed in a Pyrex test tube containing a 4-ml mixture of dimethylformamide and TEA (3:1 dimethylformamide-to-TEA volume ratio). The solution was bubbled with CO_2 (99.999%, Airgas) for 20 min prior to photocatalytic testing. An ozone-free Xe lamp (Newport) equipped with an AM 1.5 filter was used to simulate sunlight. Solar CO_2 reduction was conducted at room temperature with the reaction solution being sealed and constantly stirred. Light intensity on the reaction suspension was measured to be 220 mW/cm^2. The

20

head space above the reaction suspension was sampled with a gas-tight syringe at different time intervals for product analysis using an Agilent 7820 GC equipped with a TCD detector and a 60/80 Carboxen 1000 column.

Surface functionalized Kaolin and Aerosil 200 Silica

To investigate the photocatalytic activity of Re-L-Kaolin and Aerosil 200 Silica under visible light irradiation, 10mg of the surface functionalized catalysts were dispersed in a Pyrex test tube containing a 4-ml mixture of dimethylformamide and TEA (3:1 dimethylformamaide-to-TEA volume ratio) and 5mg of $Ru(bpy)_3^{2+}$. The solution was bubbled with CO_2 (99.999%, Airgas) for 20 min prior to photocatalytic testing. A visible light with adjustable scales (Fiber- Lite) was used as light source to mimic sunlight. Solar CO_2 reductions were conducted at room temperature with the reaction solution being sealed and constantly stirred under irradiation of different light intensities, which were measured to be 50 mW/cm^2, 100 mW/cm^2 and 150 mW/cm^2, respectively. The head space above the reaction suspension was sampled with a gas-tight syringe at different time intervals for product analysis using an Agilent 7820 GC equipped with a TCD detector and a 60/80 Carboxen 1000 column.

CHAPTER 3

SYNTHESIS AND CHARACTERIZATION OF MICRO-POROUS ZEOLITES

AND MESO-POROUS SILICAS

3.1 Synthesis of micro-porous zeolites and material characterization

As discussed in the previous section, nano zeolite materials with micro-porous structures have various applications due to the unique properties.[27,28,29,30] Synthesis of zeolites usually involves hydrolysis of starting materials, adjusting pH of reaction gels and a hydrothermal step for nucleation and zeolite crystals growth.[31,32,33,34] By adjusting composition of starting materials and hydrothermal conditions, different types of zeolites with varying morphologies and pore sizes could be obtained.[14,15,16]

3.1.1 Synthesis of micro-porous zeolite ZSM-5

ZSM-5 (Zeolite Socony Mobil–5), is an aluminosilicate zeolite mineral belonging to the pentasil family of zeolites, with a MFI (mordenite framework inverted) type structure (Figure 3.1)[17]. The chemical formula of ZSM-5 zeolite is $Na_nAl_nSi_{96-n}O_{192} \cdot 16H_2O$ (0<n<27). Several ZSM-5 synthesis methods have been reported by different researchers. [16,35,36,37] Larsen and co-workers described a crystalline ZSM-5 synthesis procedure using template methods under

hydrothermal conditions.[16] By modifying the ratio of starting materials in the

reaction gel, nano crystalline ZSM-5 with uniform structure and size, as small as

15nm could be obtained.[16] The molar ratio of Si/Al is 20 in this material, which is

much lower than that in most of the other reported ZSM-5 zeolites, the high

proportion of Al in the structure renders the hydrophilic property of the material

and according ion exchange and catalysis capabilities.

5-1
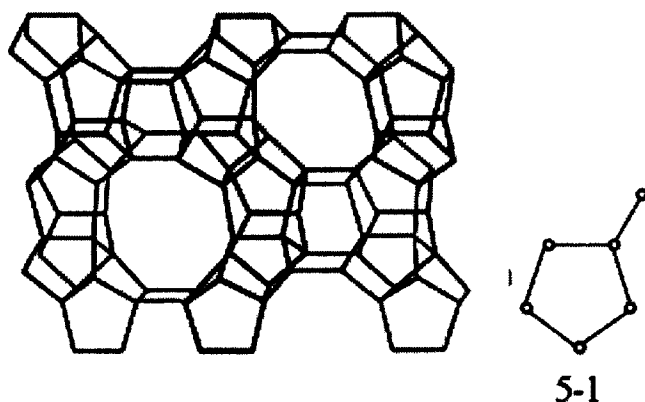
Figure 3.1 MFI zeolite structure and a 5-1 subunit [17]

In general, the synthesis in this thesis followed Larsen's procedure,[16,38]

but the specific reaction conditions like temperature and reaction time were

adjusted to adapt to our own experimental facilities. To start the synthesis,

measured amount of starting chemicals were mixed as the reaction gel, in the

molar ratio: 9TPAOH: 0.16NaOH: Al: 25Si: 495H$_2$O: 100EtOH, where TPAOH=

Tetrapropylammonium hydroxide; Al= Aluminum isopropyloxide; Si= Tetraethyl

orthosilicate. The mixture was stirred at room temperature overnight to ensure

23

aluminum isopropyloxide and tetraethyl orthosilicate completely hydrolyzed to isopropyl alcohol and ethanol, respectively. Next, the clear solution was transferred into a Teflon lined autoclave and kept at 165 °C for 120 hours for hydrothermal treatment. The synthesized ZSM-5 crystals were recovered by centrifugation and washed with deionized water at least 3 times to get rid of residual chemicals in the crystals, then dried at room temperature overnight and calcined at 600 °C for 6 hours with oxygen flow to remove the TPAOH template.

3.1.2 Synthesis of micro-porous zeolite Silicalite-1

Silicalite-1 is the pure silica analogous of ZSM-5 with MFI topology, there is no Al in the 5-1 pentagon building subunits which are connected to build the channels and interconnections of the 3D structure of zeolite crystals.[39] As shown in Figure 3.1, the 5-1 subunits represent the MO_4 tetrahedral unites of zeolites, where M is Si or Al. Compare to ZSM-5, Silicalite-1 zeolite has a higher hydrophobicity and thermal stability because of no presence of Al in its structure, which also accounts for the electrical neutral property of Silicalite-1.

In this thesis, the synthesis of silicalite-1 also followed Larsen's procedure,[38] which is very similar to the method for synthesis of the ZSM-5. The only difference between these two methods is: there is no aluminum source in the synthesis gel of Silicalite-1. The starting materials for synthesis of Silicalite-1 are: 9TPAOH: 0.16NaOH: 25Si: 495H_2O: 100EtOH (molar ratio). Then the mixture undergoes a similar procedure as that for synthesis of the ZSM-5 to obtain the Silicalite-1 material.

2.1.3 Characterization of nano-crystalline zeolites

To investigate the synthesized materials' morphologies, particle sizes, crystal structures and surface areas, the calcined ZSM-5 and Silicalite-1 zeolite crystals were characterized by using Scanning Electron Microscopy, X-ray Diffraction and Nitrogen Adsorption Isotherms.

According to the SEM images (Figure 3.2), the average particle size of the synthesized ZSM-5 is around 200nm and most of the particles have a cubic morphology, while the particles of the Silicalite-1 have an average size about 120nm, which are mostly spherical. The obtained zeolite sizes are much greater than the reported values by Larsen, which are 60nm and 20nm for ZSM-5 and Silicalite-1, respectively. It is not clear which synthesis factors caused this difference, one suggestion is the stirring speed of the crystals assembling step in my synthesis is slower than that used in the reported work. As a result, the template micelles are not well dispersed in the solution, so the silica species aggregated around the template micelles and formed much larger crystals than the well dispersed crystals. Higher room temperature in the starting materials hydrolysis step may also account for the formation of larger zeolite crystals, because higher temperature will accelerate the hydrolysis speed of aluminum isopropyloxide and tetraethyl orthosilicat. This means more aluminas and silicas are present in a shorter time; accordingly, larger clusters will be formed in the solution.
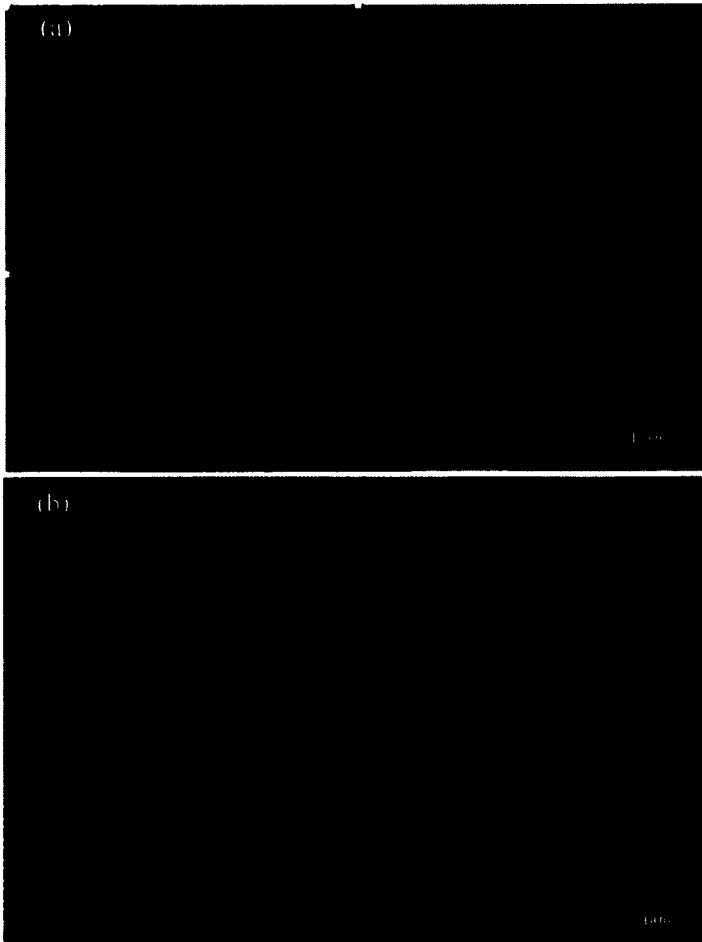
Figure 3.2 SEM images of the calcined zeolites samples: (a) ZSM-5 (200nm) and (b) Silicalite-1(120nm)

X-ray diffraction patterns of the synthesized zeolite materials were recorded over a 2Θ range from 5˚ to 40˚ with a scanning speed of 2˚ per minute and a steep size of 0.05˚, the X-ray source was operated at 35KV and 30mA. As shown in Figure 3.3, the ZSM-5 has characteristic peaks at 8.9˚, 23.2˚ and 23.5˚, while the Silicalite-1 has peaks at 8.0˚, 8.8˚, 23.2˚ and 23.5˚. Both the XRD patterns are consistent with the structures of ZSM-5 and Silicatlite-1, respectively.

Figure 3.3 XRD patterns of the synthesized zeolite samples: (a) ZSM-5 and (b) Silicalite-1

To measure the total surface areas of the synthesized zeolites, the calcined

products were measured on a Nova 2200e Surface Area & Pore Size Analyzer.

By using BET method, surface areas were obtained from the nitrogen

adsorption/desorption isotherms, which were 283 and 285m^2/g for the ZSM-5

and Silicatlite-1 zeolites, respectively. The total surface areas are also smaller than the reported values of Larsen because of larger particle sizes.

3.2 Synthesis of meso-porous silica SBA-15 and material characterization

3.2.1 Synthesis of meso-porous silica SBA-15

As discussed in chapter 1, mesoporous silica SBA-15 is an excellent catalyst support due to the thermal and chemical stability. [25,40,41] Ordered porous structure and pore size that could reach as large as 30nm are ideal for immobilization of bulky metal complexes such as rhenium bipyridyl complexes in the pore surfaces. Since Stucky and co-workers invented the synthesis method of this material,[20] numerous synthesis works have been implemented by various researchers,[42,43,44,45] although some specific reaction conditions or components of starting materials may vary, the synthesis mechanisms are the same. Scheme 3.1 illustrates the basic strategies of forming a silica material with ordered hexagonal porous structure.[46]
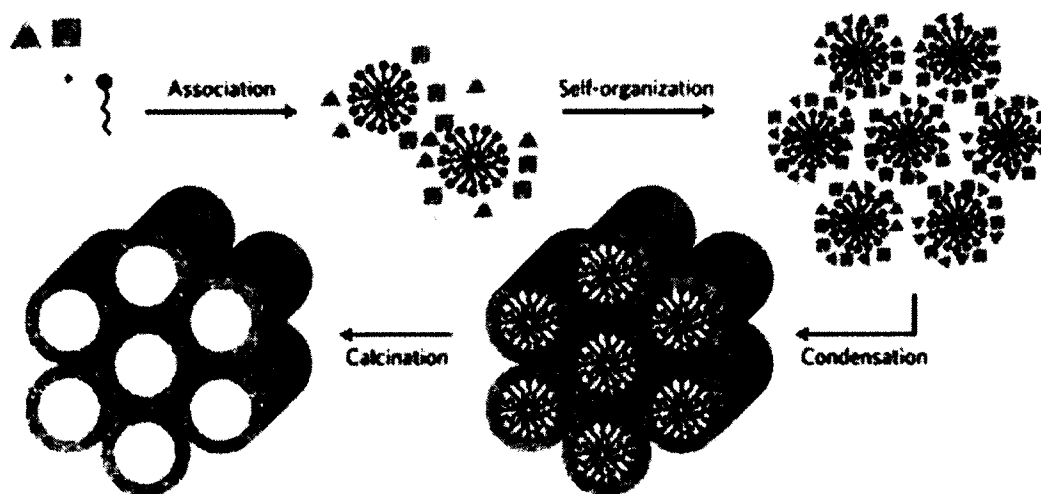
Scheme 3.1 Mechanism for the formation of SBA-15[46]

The synthesis undergoes a two-step hydro-thermal pathway. The first step

involves self-association of structure directing templates and assembling of silica

species around the template micelles at a lower temperature, whereas the

second step is the mesoporous structure expansion and silica wall consolidation

process usually under a static condition with a higher temperature. In Stucky's

procedure,[20] the template is a triblock copolymer Poly(ethylene glycol)–

poly(propylene glycol)–poly(ethylene glycol) (PEO-PPO-PEO). EO to PO ratio in

the polymer affects the morphology of resulting products. Usually, templates with

higher EO: PO ratios produce cubic mesoporous silicas, while polymers with

lower EO: PO ratios and low concentrations (0.5-1 weight %) favor a *p6mm*

hexagonal porous structure. Adding a co-template in the reaction gel will also

change the product's morphology.

In this thesis, the synthesis of the hexagonal mesoporous silica SBA-15 also followed the reported works of Stucky.[20] First, a template Poly(ethylene glycol)–poly(propylene glycol)–poly(ethylene glycol) (feed ratio EO: PO: EO is 20:70:20, average molecular weight is around 5800) and a silicon source tetraethyl orthosilicate were mixed in an acidic aqueous solution and kept stirred at a lower temperature (25-40°C) for mesoporous structure formation. Next, the cloudy mixture was transferred to a Teflon lined autoclave and aged at a higher temperature (80-230°C) for silica wall condensation. Resulting products were recovered by filtration and washed with deionized water, kept at 60°C overnight to get completely dried and calcined with O_2 flow to remove the templates and form the porous structure.

To pursue SBA-15 silicas with desired morphology and ideal pore size as a catalyst support for our photocatalytic CO_2 reduction study, several batches of SBA-15 were produced by manipulating the synthesis conditions and adjusting starting materials' composition, as described in Table 3.1.

Table 3.1 SBA-15 synthesis conditions

Batch #	Starting Materials					Step1 (self-assembling)	Step2 (hydrothermal treatment)
1	P-123 1g	HCl(1.4M) 35m l	TEOS 2.1g			Room temp. Stirring 1h	180°C, 5h 230°C,2h
2	P-123 1g	HCl(1.4M) 35ml	TEOS 2.1g			Room temp. Stirring 1h	180°C 16h
3	P-123 1g	HCl(1.4M) 35ml	TEOS 2.1g			Room temp. Stirring 1h	100°C 24h
4	P-123 1g	HCl(1.4M) 35ml	TEOS 1.5g			Room temp. Stirring 12h	80°C, 10h 120°C,12h
5	P-123 1g	HCl(0.8M) 75ml	TEOS 2.1g			Room temp. Stirring 24h	100°C 48h
6	P-123 1g	HCl(0.8M) 75ml	TEOS 2.1g			Room temp. Stirring 24h	150°C 48h
7	P-123 1g	CTAB 0.1g	HCl(1.3M) 23ml	C_2H_5OH 5ml	TEOS 2.5g	Room temp. Stirring 1h	180°C, 4h 200°C,4h
8	P-123 1g	CTAB 0.1g	HCl(1.3M) 23ml	C_2H_5OH 5ml	TEOS 2.5g	Room temp. Stirring 12h	80°C, 4h 120°C,4h

3.2.2 Characterization of meso-porous silica SBA-15

To obtain the physical properties of the synthesized silica materials, they were characterized by using Scanning Electron Microscopy and Nitrogen Adsorption/desorption Isotherms. Figure 3.4 displays the SEM images of the SBA-15 samples and clearly indicates the particle shapes and sizes of different batches.
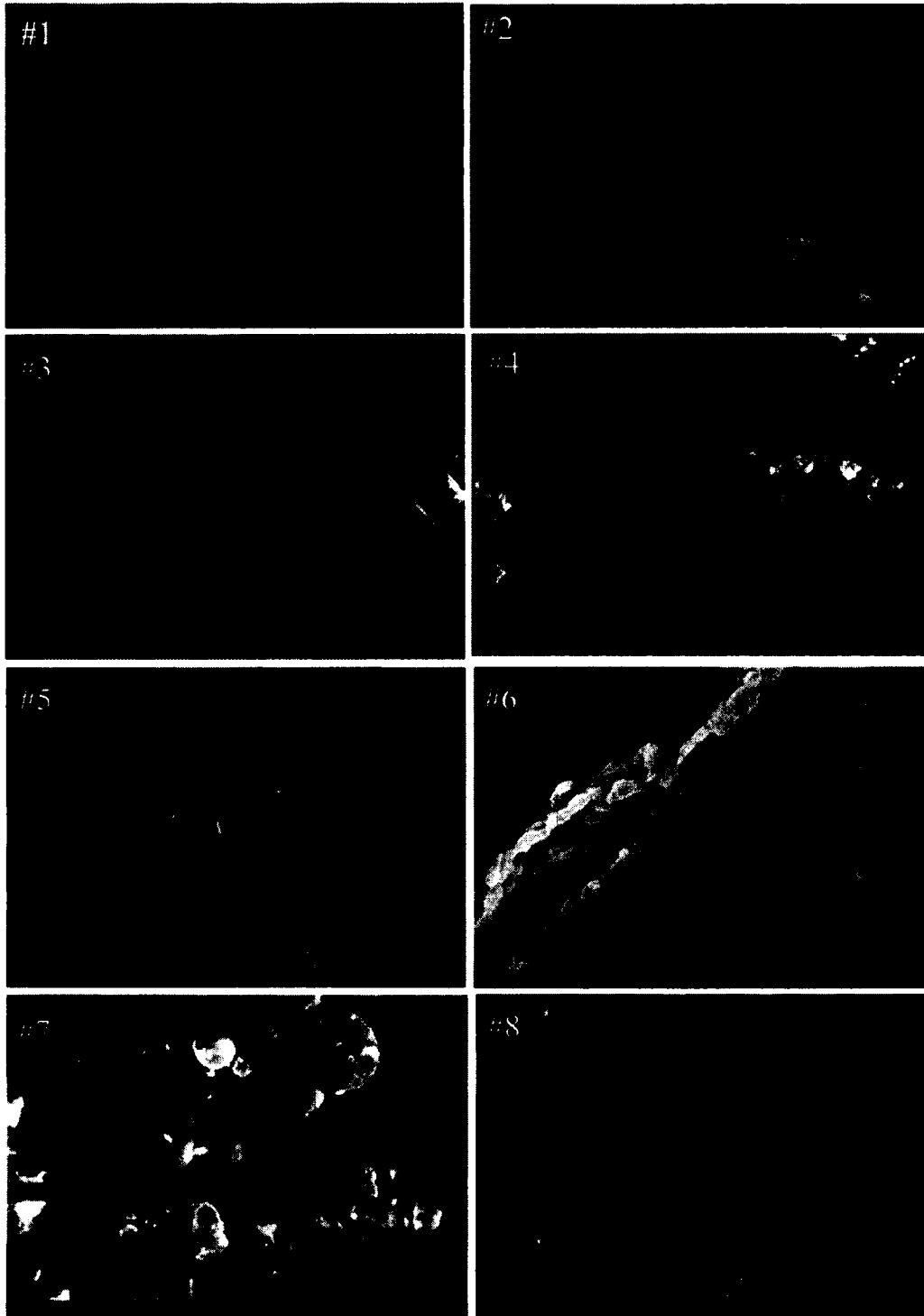
Figure 3.4 SEM images of synthesized SBA-15(batch #1-8), scale bar in #3, 4, 7, 8 represent 10μm, scale bar in #1, 2, 5, 6 represent 1μm

Figure 3.5 illustrates the Nitrogen Adsorption/Desorption Isotherm of one of the synthesized SBA-15 silicas. By using BET method, the sample's total surface area is derived from the linear range (P/P$_0$ from 0.05 to 0.30) of the adsorption isotherm, the total pore volume is calculated from the single point adsorption where P/P$_0$= 0.99 and the pore size distribution and average pore radius are obtained from the desorption isotherm using BJH method.
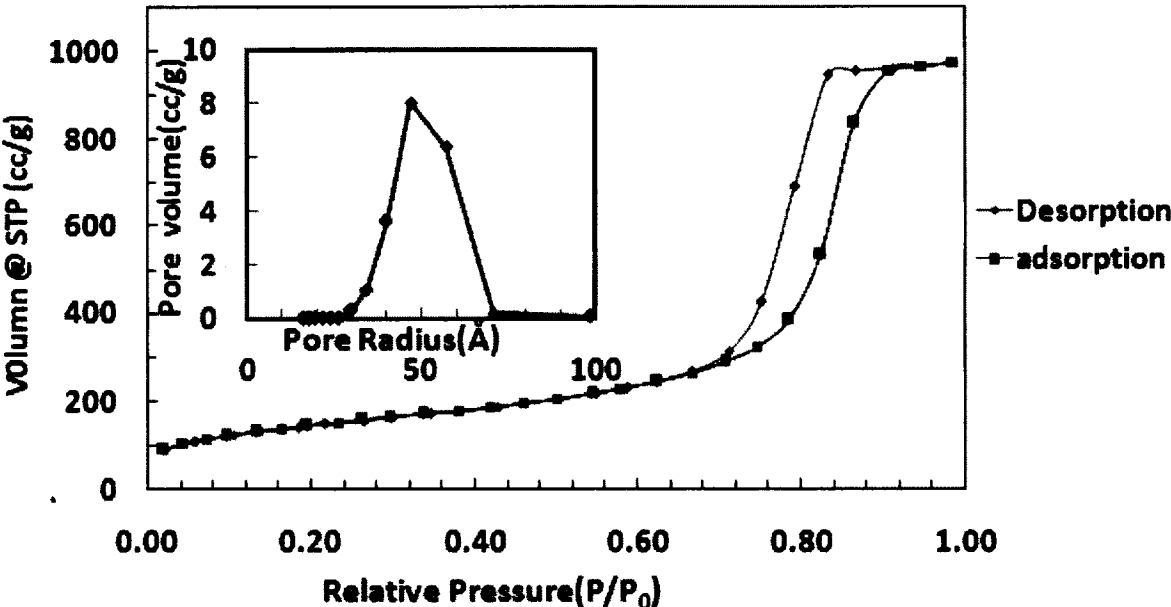
Figure 3.5 Nitrogen Adsorption/Desorption Isotherm of SBA-15 # 7, insert shows the pore size distribution

Table 3.2 BET surface areas, average pore radius and total pore volumes of the synthesized silicas

Batch #	BET surface area (m^2/g)	Average pore radius($Å$)	Total pore volume (cm^3/g)
1	226.3	44	0.55
2	326.1	48	0.94
3	327.2	27	0.44
4	846.9	34	1.2
5	479.0	27	0.99
6	357.1	49	0.99
7	510.3	47	1.5
8	864.6	24	1.2

According to the synthesis conditions shown in Table 3.1 and the coresponding products' properties shown in Table 3.2, SBA-15 silica particles' shapes and pore sizes are controllable in the synthesis; adjusting the composition of starting materials and reaction conditions will produce products with different physical properties. In general, higher temperature and longer reaction time for the hydrothermal treatment process result in larger pore sizes and thinner silica walls, because of protonation of the polymers or temperature-dependent hydrophilicity of the PEO-block. Lower molar ratio of silica source to template will generate silicas with larger pore sizes as well. Lower reaction temperatures decrease the particle size due to a slower aggregation speed of individual crystals, however longer reaction time is required to fulfill this procedure. Presence of a co-template, hexadecyltrimethylammonium bromide, in batch #7 and 8 changed the products' particle shape from rod-shaped to spherical.

3.3 Conclusions

Micro-porous zeolites ZSM-5 and silicalite-1 were synthesized in aqueous solutions by using a hydrothermal method. The obtained ZSM-5 has a relative high Al/Si molar ratio in the MFI structure, which renders it good hydrophilicity. Particle size of the synthesized ZSM-5 and Silicalite-1 are 200nm and 120nm; surface area of the synthesized ZSM-5 and Silicalite-1 are 283m^2/g and 285m^2/g, respectively. Modification of the synthesis condition is necessary to acquiring zeolites with smaller particle sizes. Two-D hexagonal packed meso-porous silica, SBA-15, was also synthesized through a hydrothermal treatment, using triblock co-polymer, P123, as the structure directing templates. Meso-porous silicas with pore radii from 2.4nm to 4.9nm were obtained by adjusting the synthesis conditions, such as concentration and molar ratio of the starting materials, reaction time and temperature of the hydrothermal treatment. Particle size and morphology of the product are also controllable by manipulating these synthesis conditions.

CHAPTER 4

SURFACE IMMOBILIZATION OF Re(BPY)(CO)$_3$CI ON MESO-POROUS

SILICA FOR SOLAR CO$_2$ REDUCTION

4.1 Introduction

As discussed in chapter 1, molecular and supramolecular complexes of

Ru, Re, Co, and Ni are homogeneous photocatalysts capable of mediating

efficient multi-electron CO$_2$ reduction. [2,11,47,48] However, the poor stability of most

homogeneous photocatalysts under photochemical conditions limits applications

and development of these catalysts. TiO$_2$-based heterogeneous photocatalysts

are robust under photocatalytic reaction conditions[23,49,50,51] but semiconductor

surfaces are usually inefficient in catalyzing multi-electron CO$_2$ reduction due to

the prevailing charge recombination in semiconductor photocatalysts. Surface

immobilization is a valid way to deal with these drawbacks. Surface-immobilized

molecular catalysts have the potential to combine the advantages of

homogeneous and heterogeneous catalysis.[24,52] Various approaches have been

developed to immobilizing molecular catalysts on solid-state surfaces for

photocatalysis, including photo CO$_2$ reduction catalysis.[53,54,55,56]

In this present study, surface immobilized tricarbonyl Re(I)-bpy, where bpy=2,2'-

bipyridine,[8] on mesoporous silicas, have been achieved via both covalent

attachment and physical adsorption. Tricarbonyl Re(I) complexes have been covalently attached to titanium dioxide surface[57] or supported in a polyoxometalate[58] for photochemical studies. Rosenfeld and co-workers prepared a tricarbonyl Re(I) compound covalently attached to silica surface and further probed interfacial dynamics and structure of the surface immobilized Re(I) catalyst with ultrafast two-dimensional infrared vibrational echo spectroscopy.[59] Recently, Wang et al. incorporated a tricarbonyl Re(I) complex in a highly stable and light-absorbing metal-organic framework, which showed significantly higher photocatalytic activity than the corresponding homogeneous complex.[60] Takeda et al. prepared a tricarbonyl Re(I) complex covalently anchored in a periodic mesoporous organosilica.[25] Enhanced CO_2-to-CO conversion was achieved on the anchored Re(I) catalyst upon UV light activation of the organosilica and subsequent resonance energy transfer. It was further demonstrated that the mesoporous structure of the organosilica protected the Re(I) complex against photochemical decomposition.[25] Microporous zeolites and mesoporous silicas have been employed as host materials for single-site titanium oxides[27,28,61,62] and oxo-bridged heteronuclear redox sites[63,64] as all-inorganic CO_2-reduction photocatalysts. Park and co-workers studied tricarbonyl Re(I) catalysts encapsulated in NaY and Al-MCM-41.[65,66,40] Under light ($\lambda > 350$ nm) irradiation, CO_2 was converted into CO and CO_3^{2-} species on the encapsulated Re(I) catalysts. The researchers assumed that zeolite frameworks acted as electron donors for CO_2 reduction.

Recently, Dubois et al. tried physical adsorption of Re-bpy in a hierarchical mesoporous ZSM-5 and investigated photochemical properties of this material.[67] A significant amount of Re-bpy was retained in the zeolite mesopores through simple liquid-phase adsorption. The molecular Re(I) catalyst was then tested in photochemical CO_2 reduction at the gas-surface interface in the presence of co-adsorbed $Ru(bpy)_3^{2+}$ photosensitizer and an amine-based electron donor. Upon visible-light irradiation, the formation of important reaction intermediates, including Re-carboxylato and Re-formato species, was demonstrated by using in situ Fourier transform infrared spectroscopy (FTIR).

This present study compared covalent attachment with physical adsorption as strategies for immobilization of Re-bpy on mesoporous silica. Spectroscopic techniques, including FTIR and UV–visible spectroscopies, are employed to characterize the surface immobilized Re(I) photocatalysts. In comparison with physical adsorption, covalent attachment should be more robust and could retain more Re(I) centers in the mesoporous materials. It is also expected that the surface-immobilized Re(I) photocatalyst will demonstrate improved photocatalytic activity than its homogeneous counterpart.

4.2 Surface immobilization of the Re(I) catalyst on meso-porous SBA-15

4.2.1 Covalent attachment of Re(I) catalyst on SBA-15 silica

The covalent attachment was achieved by modifying the synthesis procedure reported by Chen et al.[68,41] as described in Scheme 4.1. First, the 2,2′-

bipyridine-4,4'-dicarboxylic acid was refluxed in $SOCl_2$ under N_2 atmosphere for 24 h and dried under vacuum to remove excess $SOCl_2$ and any generated amounts of HCl or SO_2. The resulting product, 4,4'-bis(chlorocarbonyl)-2,2'-bipyridine, was mixed with TEA and APTMS in chloroform and refluxed under N_2 for 1 h. A solution of the synthesized 4,4'-bis(3-trimethoxysilylpropyl)amido-2,2'-bipyridine in chloroform was mixed with the SBA-15 SiO_2. The mixture was allowed to stir for 2 days at room temperature before the functionalized SiO_2 was filtered and washed with chloroform, methanol, and diethyl ether, and dried overnight at 40 °C to form SiO_2-L. In order to synthesize SiO_2-L-Re, the obtained SiO_2-L and pentacarbonyl chlororhenium(I) were dispensed in toluene and refluxed overnight. The final product was filtered, washed with toluene and dichloromethane, and dried overnight at 40 °C to yield a yellow powder.
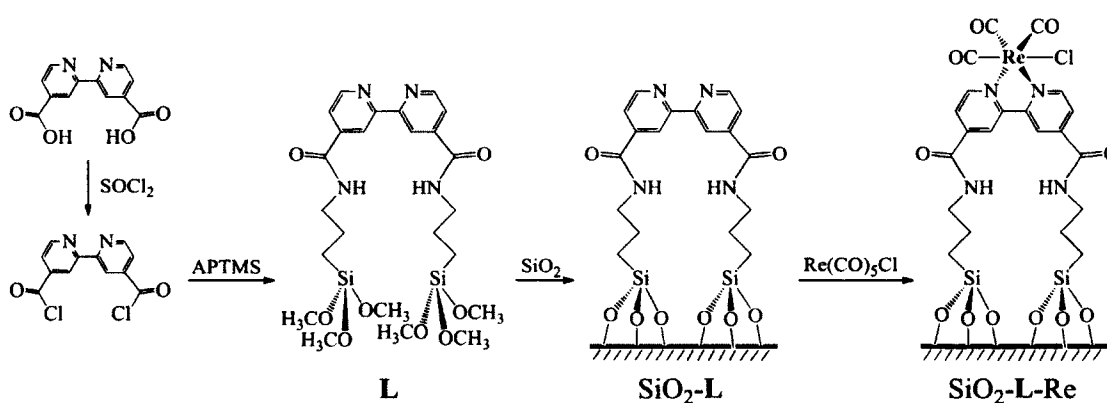
Scheme 4.1 Covalent attachment of a molecular Re(I) photocatalyst on mesoporous silica. APTMS: 3-aminopropyltrimethyloxysilane

39

4.2.2 Physical adsorption of Re(I) catalyst on SBA-15 silica

In this approach, mesoporous SiO_2 was dispersed into a solution of toluene containing Re-bpy, which was synthesized following the method described by Smieja and Kubiak.[78] After refluxing overnight, the product was filtered, washed with toluene and diethyl ether, and dried overnight at 40 °C to yield a slightly yellow powder ("SiO_2 + Re", Scheme 4.2a).
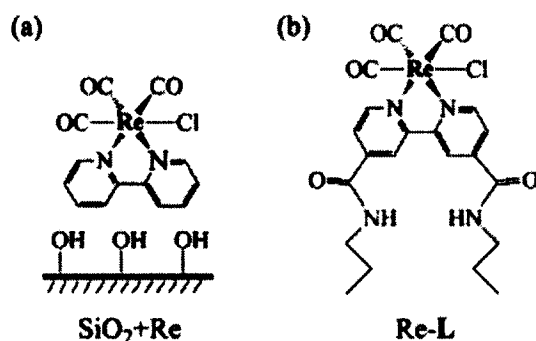
Scheme 4.2 Structures of (a) physically adsorbed Re-bpy ("SiO_2 + Re") and (b) Re-L

4.3 Characterization of the surface immobilized Re(I) catalyst on SiO_2

The as synthesized SiO_2-L-Re and SiO_2+ Re were characterized with FTIR and UV–visible spectroscopies and the amounts of Re(I) centers in SiO_2 + Re and SiO_2-L-Re were determined by elemental analysis.

4.3.1 UV-Vis Spectra of the functionalized SiO₂
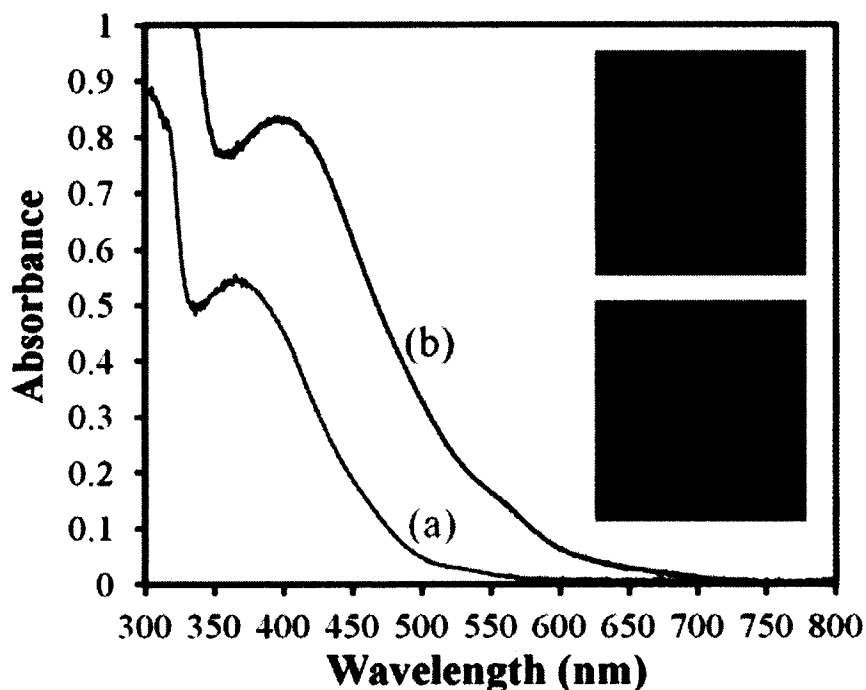
Figure 4.1 UV–visible spectra of (a) SiO₂ + Re and (b) SiO₂-L-Re in powder form. Photographs of the two samples are also shown (inset)

According to the UV-Vis spectra of the functionalized SiO₂ samples as displayed in Figure 4.1, SiO₂ + Re and SiO₂-L-Re display different colors. The synthesized SiO₂ is a white powder, which does not absorb visible light in the range between 400 nm and 800 nm. The SiO₂ sample containing physically adsorbed Re-bpy ("SiO₂ + Re") has a light yellow color, corresponding to a broad band at 365 nm in its UV–visible spectrum (Figure 4.1a). The band at 365 nm is attributed to the metal-to-ligand charge transfer (MLCT) transition of Re-bpy. The covalently

attached Re(I) complex, SiO₂-L-Re, has an intense yellow color associated with an MLCT band at 400 nm (Figure 4.1b).

4.3.2 FTIR of the synthesized materials
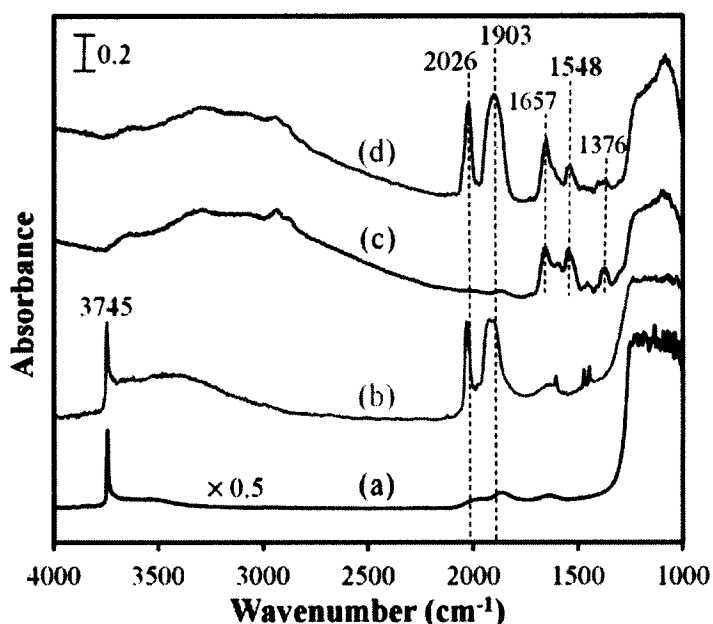
Figure 4.2 FTIR spectra of (a) SiO₂, (b) SiO₂+Re, (c) SiO₂-L, and (d) SiO₂-L-Re. The spectra were collected at room temperature under argon atmosphere

Figure 4.2 shows the FTIR spectra of the mesoporous SiO_2 with and without surface functionalization. An intense absorption at 3745 cm^{-1} featuring surface silanol (SiOH) groups is present in the spectrum of SiO_2 (Figure 4.2a). The silanol peak is also seen in the FTIR spectrum of SiO_2 + Re (Figure 4.2b), which

does not contain covalent bonds between the SiO_2 surface and the physically

adsorbed Re-bpy (Scheme 4.2a). However, the peak at 3745 cm^{-1} is not present

in the spectrum of SiO_2-L (Figure 4.2c) or SiO_2-L-Re (Figure 4.2d), in which the

SiO_2 surface is functionalized with the silane coupling agent (see Scheme 4.1).

The spectra of SiO_2-L and SiO_2-L-Re also contain other infrared features,

particularly the three peaks associated with the amide linkages at 1376 cm^{-1} (C-

N stretch), 1548 cm^{-1} (N-H bend) and 1657 cm^{-1} (C-O stretch) as well as the

methylene C-H stretching bands around 2800–3000 cm^{-1} (not labeled, Figure

4.2c and d). Comparison of the infrared spectra shown in Figure 4.2 clearly

demonstrates that covalent attachment of ligand L was achieved by reacting of

the silane coupling agent with surface silanol groups. It should be pointed out

that hydration of silica surfaces could also lead to the disappearance of the peak

at 3745 cm^{-1} characteristic of isolated silanol groups. In our study, surface

immobilization of ligand L was carried out in chloroform under ambient conditions.

Neither of the spectra of the surface functionalized silica (Figure 4.2c and d)

contains an intense absorption at 1630 cm^{-1} characteristic of surface adsorbed

water molecules, suggesting minimal hydration of the silica surface. Therefore,

the absence of the peak at 3745 cm^{-1} in the spectra shown in Figure 4.2c and d

is mostly due to the depletion of silanol groups upon surface functionalization

according to Scheme 4.1. This is further supported by the absence of

absorptions in the range of 2815–2850 cm^{-1} (C-H stretch of methoxy groups) in

the spectra of the functionalized silica.

Two broad absorptions at 1903 cm^{-1} and 2026 cm^{-1} characteristic of surface Re-carbonyl groups[25,60] and are present in the spectrum of SiO_2-L-Re (Figure 4.2d), indicating the tricarbonyl Re(I) catalyst was successfully anchored on SiO_2 through covalent linkages according to the strategy described in Scheme 4.1. The two Re-carbonyl bands are also seen in the spectrum of SiO_2 + Re (Figure 4.2b), suggesting a certain amount of Re-bpy remained adsorbed in the mesoporous SiO_2 even in the absence of covalent linkages between the Re(I) complex and the SiO_2 surface. The same spectrum contains several less intense absorptions between 1400 cm^{-1} and 1600 cm^{-1} associated with the bpy ligand of Re-bpy (Figure 4.2b, not labeled).

4.4 Photocatalytic CO_2 reduction using the surface immobilized Re(I) catalyst
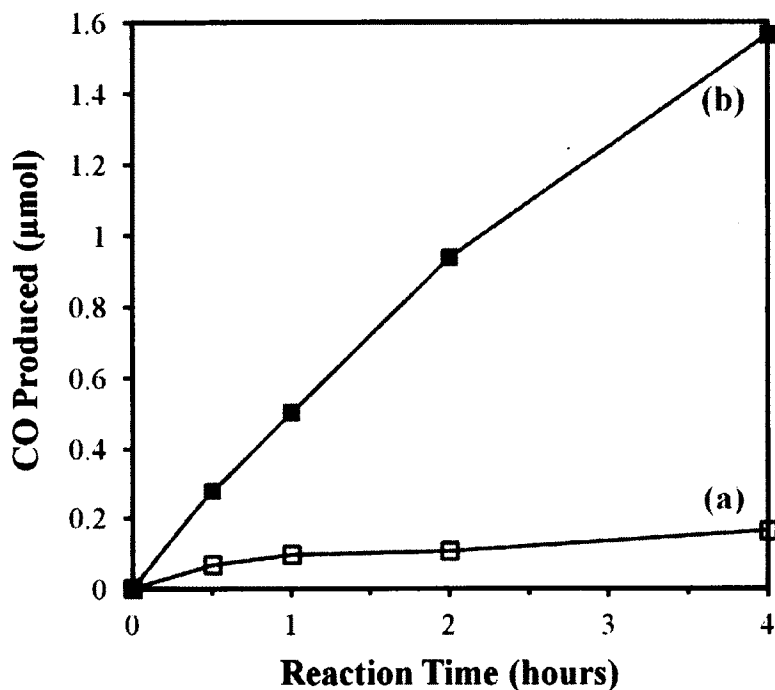
Figure 4.3 Photocatalytic activities of (a) SiO_2+Re and (b) SiO_2-L-Re in solar CO_2 reduction. The amounts of CO produced were normalized to 10 mg of functionalized SiO_2 samples.

To compare the photocatlytic activity of the surface functionalized SBA-15 silicas by different approaches, both SiO_2 + Re and SiO_2-L-Re were tested in solar CO_2 reduction under same reaction condition. The photocatalytic activities of these two samples were illustrated by showing the amount of CO produced during the test as a function of reaction time, as shown in Figure 4.3. According to the

amount of CO generated by the reactions, the covalently attached SiO_2-L-Re demonstrated significantly higher activity than SiO_2 + Re in solar CO_2 reduction. The amount of CO produced using SiO_2-L-Re was ~10 times greater than that using SiO_2 + Re under the same experimental conditions for 4 h. Obviously, the better photocatalytic performance of SiO_2-L-Re relative to SiO_2 + Re partly resulted from the higher Re(I) content in the former (5.1 μmol/ 10mg powder) than the latter (1.5 μmol/ 10mg powder). Another possible reason should be the greater photoresponse of SiO_2-L-Re in the visible region Since photochemical CO_2 reduction on tricarbonyl Re(I) catalysts is initiated by the MLCT transitions, SiO_2-L-Re could harvest more photo (Figure 4.1). As mentioned earlier, the MLCT transitions for the Re(I) centers in SiO_2-L-Re and SiO_2 + Re were found to be at 400 nm and 365 nm, respectively. Since photochemical CO_2 reduction on tricarbobyl Re(I) catalysts is initiated by the MLCT transition, SiO_2-L-Re can harvest more photonic energy than SiO_2 + Re in the visible-light region.
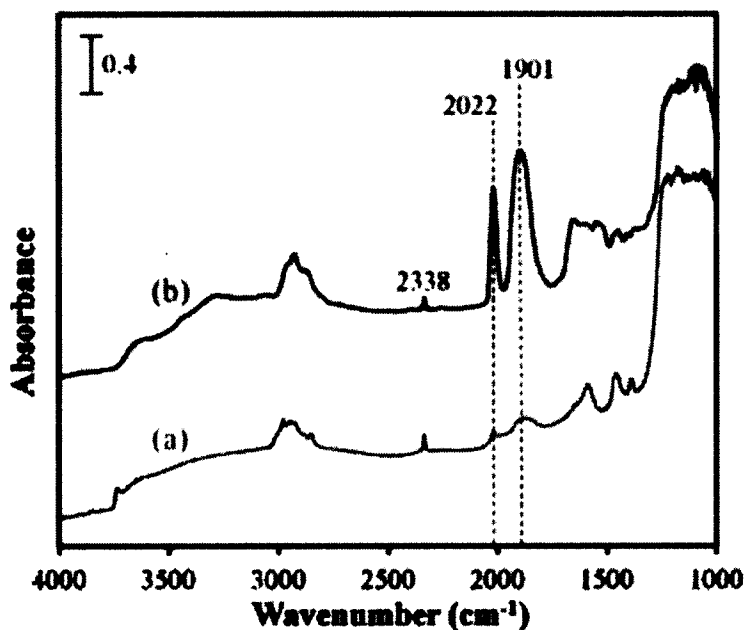
Figure 4.4 FTIR spectra of (a) SiO_2 + Re and (b) SiO_2-L-Re after solar CO_2 reduction in a solution of acetonitrile containing triethylamine for 4 hour

The excellent stability of SiO_2-L-Re under photochemical conditions also contributed to its higher activity than SiO_2 + Re. Figure 4.4 shows the FTIR spectra of both samples after solar CO_2 reduction in acetonitrile for 4 h followed by washing with acetonitrile and drying at room temperature. Two intense absorptions at 1901 cm^{-1} and 2022 cm^{-1} characteristic of Re-carbonyl, together with the absorption peaks associated with the amide linkages (1376 cm^{-1}, 1548 cm^{-1} and 1657 cm^{-1}, not labeled), are clearly seen in the spectrum of used SiO_2-L-Re (Figure 4.4b). The presence of these absorption features indicates a significant amount of tricarbonyl Re(I) centers remained covalently attached to SiO_2 after the photocatalytic reaction. This is consistent with the study by Takeda et al.[11] suggesting that mesoporous structures could protect the Re(I) complex

against photochemical decomposition. In contrast, only negligible intensity Re-carbonyl absorption features are seen in the spectrum of used SiO_2 + Re, shown in Figure 4.4a. It can be concluded that the majority of Re-bpy in SiO_2 + Re decomposed during photocatalysis and/or were washed off the SiO_2 surface. An absorption peak at 2238 cm^{-1} as well as C-H stretching bands near 3000 cm^{-1} (not labeled) associated with surface adsorbed CO_2 and hydrocarbons, respectively, are also present in the spectra of both functionalized SiO_2 after photocatalytic reactions.

The CO_2-reduction activity of SiO_2-L-Re was also compared with the derivatized homogeneous complex, Re-L, in order to probe the effect of surface immobilization. Upon light irradiation for 4 h, 2.2µmol of CO was produced by a suspension containing 10 mg of SiO_2-L-Re in comparison to 1.7µmol of CO produced by a dimethylformamide solution containing 5.1µmol of Re-L. Since there are ~5.1µmol of Re(I) centers in 10 mg of SiO_2-L-Re, it is concluded that surface immobilization on mesoporous SiO_2 enhanced (or at least did not negatively influence) the activity of the homogeneous Re(I) complex in solar CO_2 reduction.

*FTIR spectra were taken by my lab colleague Kevin Dubois; photocatalytic tests were performed by my lab colleague Chao Liu.

4.5 Conclusions

In summary, we have immobilized a tricarbonyl Re(I) photocatalyst on mesoporous silica via both covalent attachment and physical adsorption. The covalent attachment was achieved by derivatizing the bpy ligand with amide linkages connected to silane coupling agents, which was then immobilized on silica prior to complexation of bpy with Re(I). Derivatization of the bpy ligand with amido moieties resulted in a 35-nm red shift in the MLCT transition of the tricarbonyl Re(I) complex. Such a red shift into the visible light region is advantageous for photocatalysis using natural sunlight. When tested in solar CO_2 reduction, the covalently attached photocatalyst demonstrated excellent stability and higher activity than both its homogeneous counterpart and the physically adsorbed Re(I) photocatalyst. Most likely, the mesoporous structure protected the Re(I) complex against photochemical decomposition and therefore enhanced the photocatalytic activity of the covalently attached Re(I) complex.

CHAPTER 5

SURFACE IMMOBILIZATION OF Re(BPY)(CO)₃Cl ON KAOLIN FOR SOLAR

CO_2 REDUCTION

5.1 Introduction

Nanoporous materials, such as nanoporous silicas and zeolites, are popular candidates as solid-state catalyst supports and have been investigated in various catalytic reactions.[69,70] The hexagonal mesoporous silica SBA-15 exhibits excellent performance in our solar CO_2 reduction reactions due to the thermally and chemically stable porous structures of the silicas, which can protect the catalyst molecules and prevent them from being decomposed under photoreaction conditions. However, other structured nano materials used as catalyst supports for solar CO_2 reduction are seldom reported. One of the clay materials, Kaolin has aroused our interest in the catalyst immobilization research. Kaolin is a white mineral belongs to the clay family.[71] The name is derived from the Chinese mountain *Kao-ling*, where the Kaolin mineral was first found, so Kaolin is also called China clay. The unique properties of Kaolin make it an important industrial material. Except for being used in porcelain manufacturing, Kaolin also has multiple applications in other industrial areas such as the pharmaceutical, cosmetic, plastic, paper, as well as petroleum production.[71]

The chemical composition of Kaolin can be expressed as $Al_2Si_2O_5(OH)_4$ or $Al_2O_3 \cdot 2SiO_2 \cdot 2H_2O$, but it is not a simple mixture of amorphous silica and alumina. Instead, Kaolin is built by one tetrahedral siloxane surface and one octahedral aluminum hydroxide surface, which are linked through oxygen atoms to form the 1:1 layered crystalline construction.[26] Kaolin is chemically inert in a relatively broad pH range, but it is not as thermally stable as silica materials because Kaolin undergoes a dehydroxylation process between 200°C to 900°C and its crystalline structure will be collapsed due to the loss of hydroxyl groups.[72,73] Silica only has surface silanol groups, while Kaolin composed of multiple types of –OH groups that exit in the flaky structures. The orientations of hydroxyl groups in Kaolin have been studied via both experimental and computational methods.[26, 74,75] There are four hydroxyls in Kaolin's formula, one is in the plane of shared oxygen atoms and designated as inner hydroxyl; the other three are designated as inner surface hydroxyls because they form the outer surface of the octahedral alumina sheet. Although there are some discrepancies about bond angles and bond lengths of the hydroxyl groups between theoretical values and experimental results, the consensus is the inner hydroxyl horizontally lies on the face between the silica sheet and alumina sheet, while the three inner surface hydroxyls tilt toward the octahedral site with different angles. Figure 5.1 demonstrates the kaolinite structure according to White and co-workers' computational study.[26] According to the structure, the inner surface hydroxyls are potential functional sites that can be utilized in surface immobilization.
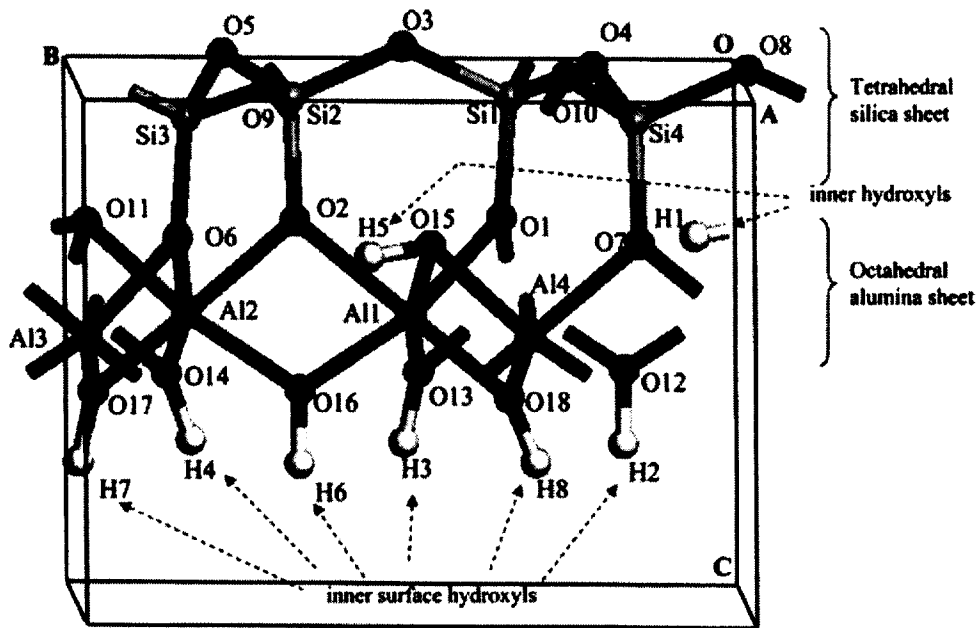
Figure 5.1 A 34-atom unit cell of kaolinite composed of silicate tetrahedral sheet, alumina octahedral sheet and hydroxyl groups[26]

In this present study, we covalently attached the Re-bpy catalyst on Kaolin surface by using the same surface immobilization strategy as that for functionalization of mesoporous silica. The bright yellow color of the surface functionalized Kaolin indicates that remarkable amount of Re-bpy was retained on Kaolin through the covalent bonds. UV-Visible and FTIR spectroscopies were employed to characterize the immobilized Re-bpy-Kaolin and revealed the differences between the Re-bpy-Kaolin and the Re-bpy-SiO$_2$ photocatalyst, which was discussed in the previous chapter. The functionalized Kaolin catalysts also exhibited some new features in the *in situ* FTIR study, which may associate with the layered structures and different hydroxyl groups in the supporting material, Kaolin. To compare with the physically adsorbed Re+ silica

photocatalyst, the physical mixing strategy was also applied to Kaolin and Re-bpy to try to get the physically adsorbed Re+ Kaolin. However, after one time of washing, the color on the obtained mixture was completely gone. UV-Visible and FTIR spectra also confirmed that there was no Re-bpy retained on Kaolin by the physical mixing method.

5.2 Surface immobilization of the Re(I) catalyst on Kaolin

5.2.1 Covalently attachment of the Re(I) catalyst on Kaolin

The immobilization strategy is according to the procedure that is used for immobilization of Re(I) catalyst on silica surface, as described in chapter 4 (scheme4.1). After obtaining the 4,4'-bis(3-trimethoxysilylpropyl)amido-2,2'-bipyridine in chloroform, Kaolin was added to the chloroform solution and the mixture was stirred for 2 days at room temperature before the functionalized Kaolin was washed with chloroform, methanol, and diethyl ether, and dried overnight at 40 °C to form Kaolin-L. Then the "as synthesized" Kaolin-L and a small portion of pentacarbonyl chlororhenium(I) was dispensed into toluene and refluxed overnight. The final product was washed with toluene and dichloromethane, and dried overnight at 40°C to yield a light yellow powder, denoted as Re-L-Kaolin.

5.2.2 Physical adsorption of Re(I) catalyst on Kaolin

The physical adsorption method is the same as that for producing SiO_2+

Re. First, Kaolin particles were dispersed in a toluene solution that containing

Re-bpy; next, the mixture was refluxed overnight and recovered by centrifugation

to get a light yellow powder. However, after washing with diethyl ether, the yellow

color in the product completely disappeared. UV-Vis and FTIR spectra of the

washed product are identical to the spectra of pure Kaolin, which indicate no Re-

bpy molecules are retained on Kaolin after washing. The reason that accounts for

this is Kaolin does not have the "cage-like" porous structures as in mesoporous

silicas; the layered structure of Kaolin can't restrain molecules effectively without

any specific interactions between the surfaces and the molecules. In conclusion,

the Re-bpy catalyst was not successfully immobilized on Kaolin by the physical

adsorption approach.

5.3 Characterization of the Re(I) catalyst on Kaolin

The product of the covalent attachment synthesis, Re-L-Kaolin, was

characterized with SEM, UV-Vis and FTIR spectroscopies and the amount of

Re(I) centers in Re-L-Kaolin was detected via elemental analysis.

5.3.1 SEM of the Re(I) catalyst on Kaolin
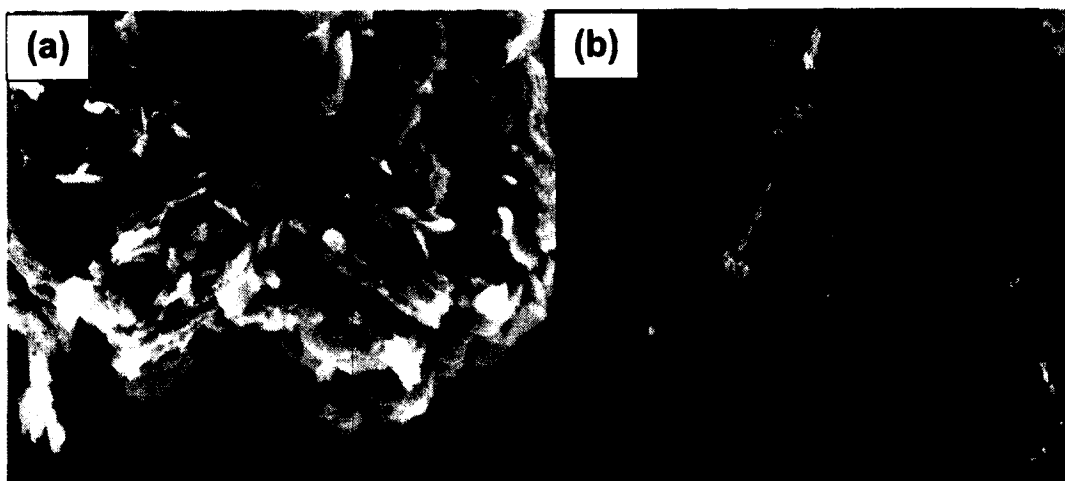
Figure 5.2 SEM images of (a) Kaolin and (b) Re-L-Kaolin (Scale bar: 1µm)

Figure 5.2 shows the SEM images of Kaolin particles and surface functionalized Kaolin. According to Figure 5.2a, the layered clay sheets are clearly seen in the SEM image and the average particle size is about 500 nm. Comparison of the two SEM images shows that the surface functionalized Kaolin maintains the layered structure and particle size with the existence of Re-L on the surfaces (Figure 5.2b).

5.3.2 UV-Vis spectrum of the Re(I) catalyst on Kaolin

The UV-Vis spectra (Figure 5.3) shows that the pure Kaolin sample does not have any absorbance in the visible light range (400nm to 800nm), while the

synthesized Re-L-Kaolin exhibits a broad absorption band at 400nm (Figure 5.3b). This absorption wavelength coincides with the absorbance peak position of the Re-L-SiO$_2$, which is also at 400nm (Figure 4.1b). Both of the absorbance peaks are due to the metal-to-ligand charge transfer (MLCT) of Re-bpy. This absorption peak indicates the functionalized Kaolin catalyst has the ability to absorb visible light and get excited for charge separation during photocatalytic reactions.
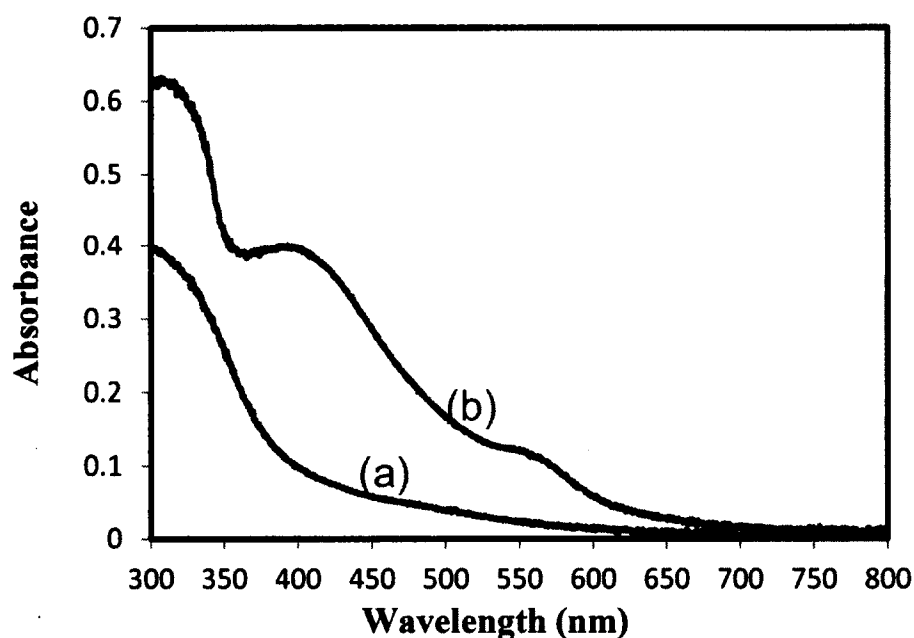
Figure 5.3 UV-Visible spectra of (a) Kaolin and (b) Re-L-Kaolin in powder form

5.3.3 FTIR of the Re(I) catalyst on Kaolin

The FTIR spectra of Kaolin before and after the surface functionalization were collected on a Nicolet iS10 FTIR spectrometer equipped with attenuated-

total-reflectance (ATR) accessory, as shown in Figure 5.4. After functionalization, the Re-L-Kaolin displays two strong absorbance at 2020 cm^{-1} and 1890 cm^{-1} (Figure 5.4b), which are the characteristic peaks of surface carbonyl groups.[25,60] These features indicate that the tricarbonyl rhenium (I) catalyst was successfully immobilized on Kaolin through the covalent linkages described in the previous chapter (Scheme 4.1). The other infrared features, especially the peaks corresponding to the amide linkages at 1636 cm^{-1} (C-O stretch); 1517 cm^{-1} (N-H bend) and 1342 cm^{-1} (C-N stretch), confirm the existence of the covalent linkages in the Re-L-Kaolin catalyst. In comparison with the infrared spectrum of the Re-L-SiO$_2$ (Figure 4.2d), the carbonyl peaks and the amide linkage peaks of the functionalized Kaolin slightly shift to lower wavenumbers with varying degrees. Both the nano-structures of supporting materials and the types of surface hydroxyl groups account for these shifts. The Re(I) catalyst molecules in the functionalized silica material are immobilized in the nanoporous environment through the covalent bonds linked with surface silanol groups, while the catalyst molecules in the functionalized Kaolin are trapped between the clay layers through the linkages with inner surface hydroxyls on the alumina surfaces.

On the infrared spectrum of the Re-L-SiO$_2$ (Figure 4.2d), it is observed that there is no surface silanol absorbance, which is a strong sharp peak at 3745cm^{-1} present in the spectrum of the pure silica (Figure4.2a). The absence of silanol peak is due to the loss of all the surface silanol groups after the surface functionalization. However, the infrared peaks associated with the surface hydroxyl groups at 3620 cm^{-1}, 3650 cm^{-1}, 3668 cm^{-1} and 3689 cm^{-1} are present in

each spectrum of both Kaolin and surface functionalized Kaolin (Figure 5.4). The reason for this is that the amount of surface hydroxyl groups in Re-L-Kaolin is much more than the amount of the linked Re (I) catalyst molecules and only a small portion of hydroxyls are taken over by the Re(I) molecules. As a result, the change of the hydroxyl absorption peaks is barely seen in the two spectra.
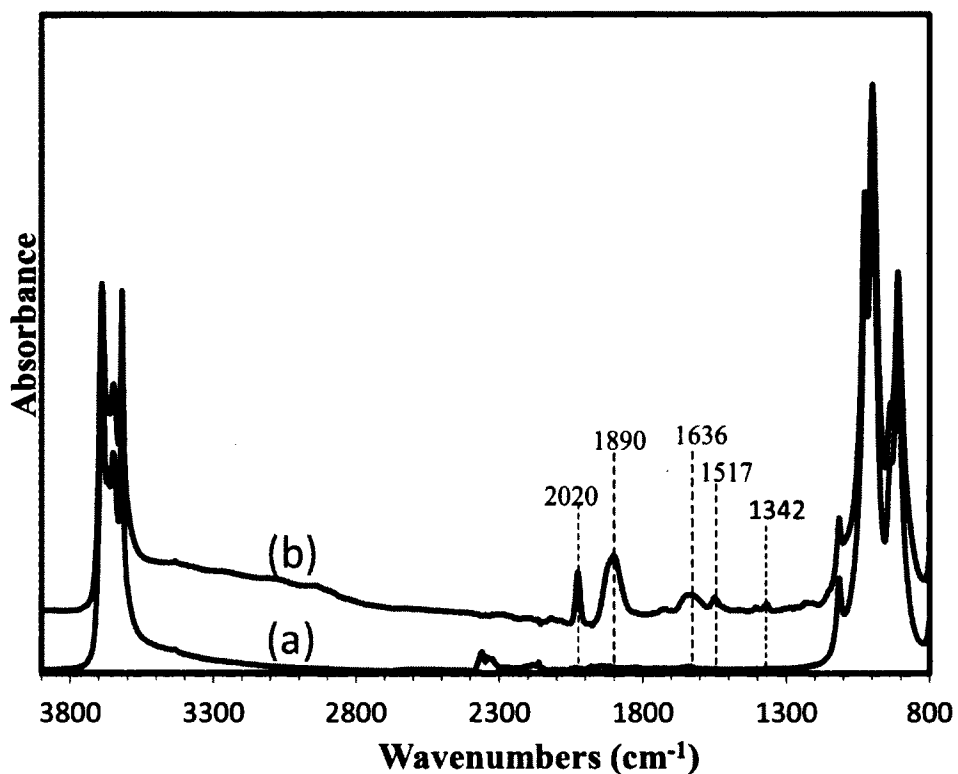
Figure 5.4 FTIR spectra of (a) Kaolin and (b) Re-L-Kaolin

5.4 Photocatalytic CO_2 reduction of the Re(I) catalyst on Kaolin

The photocatalytic activity of the synthesized Re-L-Kaolin was detected in a solution state solar CO_2 reduction procedure with the presence of a

photosensitizer, Tris(2,2'-bipyridyl)dichlororuthenium(II) complex. In this study, a Fiber-Lite series 180 visible light lamp was used to imitate solar light, giving the irradiation wavelengths >425 nm. To investigate how the intensity of input light affects the activity of the catalyst, visible light with different intensities, measured as 50 mW/cm^2, 100 mW/cm^2 and 150 mW/cm^2 respectively, were employed as input energy in the photocatalytic reactions. The amount of CO generated during the photo CO_2 reduction processes was monitored, using a gas chromatograph equipped with a TCD detector.

Figure 5.5 illustrates the activities of the as synthesized photocatalyst under 3 different irradiation intensities, by showing the CO turnover numbers as a function of reaction time. CO turnover number at each time interval is calculated using the amount of produced CO (mole) divided by the amount of Re(I) center in the reaction system (mole). According to the testing results, in the first hour, Re-L-Kaolin produced the largest amount of CO under the 150 mW/cm^2 visible light irradiation (Figure 5.5c), but after 1 hour there was no more CO generated in this system, which indicated the catalyst lost its activity after 1 hour of high intensity irradiation. When under a relatively low intensity irradiation (50 mW/cm^2 or 100 mW/cm^2), the catalyst can keep its activity in 10 hours (Figure 5.5a and b). The best performance for produce CO was acquired under the 100 mW/cm^2 irradiation, which gave a CO turnover number of 7.6 in 10 hours (Figure 5.5b).

59
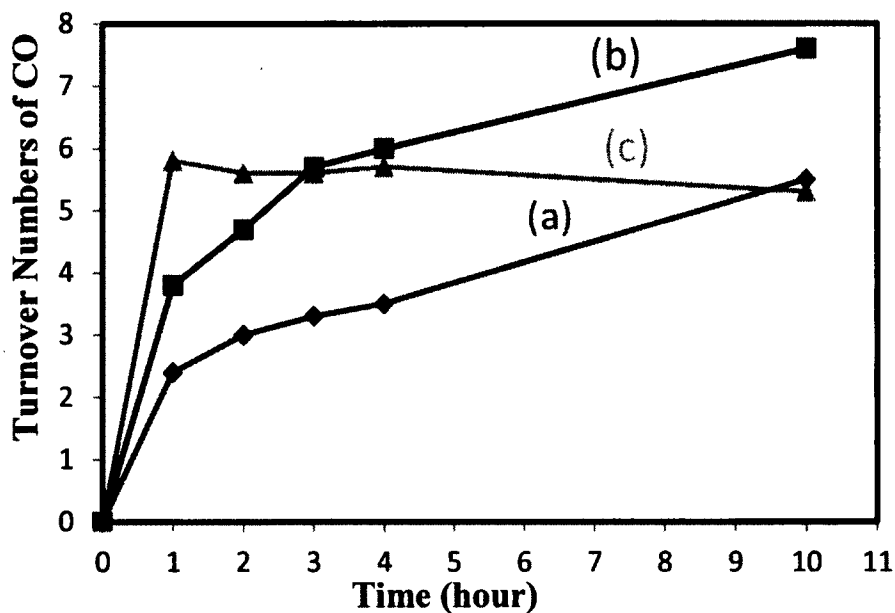
Figure 5.5 CO TONs of Kaolin-L-Re vs. time under different visible irradiation Intensity: (a) 50 mW/cm^2, (b) 100 mW/cm^2 and (c)150 mW/cm^2 (*CO TON= moles of generated CO / moles of Re(I) catalyst)

Recently, Liu et al. investigated the photocatalytic CO_2 reduction activity of the homogeneous Re-L under a similar reaction condition.[76] They obtained a CO turnover number of 14 for the homogeneous Re-L, but the homogeneous catalyst lost its activity after 2 hours reaction.[76] In this study, the surface immobilized catalyst, Re-L-Kaolin, exhibited much better stability under the photoreaction conditions. Figure 5.6 shows the FTIR spectra of the functionalized Kaolin catalyst before and after 3 different photoreactions (different intensity irradiation) in dimethylformamide solution for 10 hours. After the photoreactions, the catalysts were recovered by centrifugation, washing with acetonitrile and drying at room temperature in dark. The two strong peaks at 2020 cm^{-1} and 1890

cm^{-1}, which associate with rhenium carbonyl groups and the absorption peaks

corresponding to the amide linkages at 1636 cm^{-1},1517 cm^{-1} and 1342 cm^{-1} are

all present in the spectra of the samples that were recovered after photoreactions

(Figure 5.6a, b and c). These infrared spectra reveal the excellent stability and

recyclability of the Re-L-Kaolin under our photoreaction conditions. These

features also indicates that the layered structures of Kaolin can effectively protect

the Re (I) catalyst during the photo CO_2 reduction process.
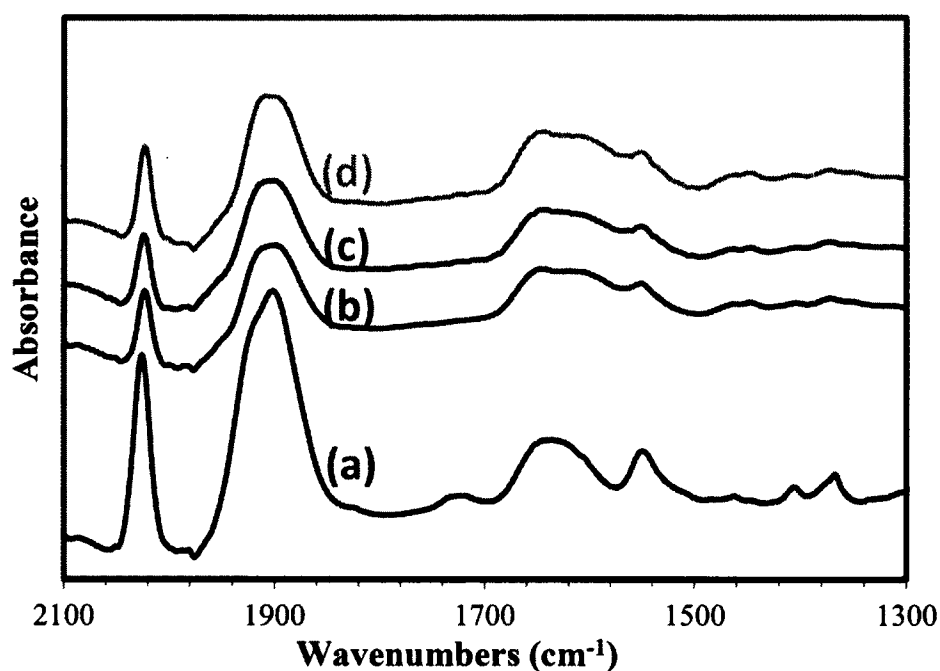
Figure 5.6 FTIR Spectra of Kaolin-L-Re after different light intensity
photocatalytic reactions: (a) before photoreaction, (b) 50 mW/cm^2, (c) 100
mW/cm^2 and (d) 150 mW/cm^2

5.5 In situ FTIR study of CO_2 reduction of covalently attached Re(I) catalyst on Kaolin

As discussed in early part, the unique 1:1 layered structure and the diversity of inner surface hydroxyls in Kaolin have brought our interest to investigate the structural and catalytical properties of the surface immobilized Re-L-Kaolin in the photocatalytic CO_2 reduction process. My lab colleague Dubois has investigated the properties of a physically mixed catalyst, $Re(bpy)(CO)_3Cl$ + mesoporous ZSM-5, during the CO_2 reduction process, using in situ FTIR spectrometry.[67] In this present study, in situ FTIR was also employed to investigate the properties of the solid state Re-L-Kaolin catalyst in the presence of a sacrificial electron donor, TEOA.

To study the structural effects of different supporting materials to the Re (I) complex, a non-porous fumed silica nano material, Aerosil 200, was also functionalized with the Re (I) compound, using the same immobilization strategy as that for synthesis of Re-L-Kaolin. The synthesized catalyst was denoted as Re-L-NPSiO$_2$ (NP means non-porous). This synthesis was performed by Kevin Dubois and the Re (I) loading on the fumed silica was determined as 2.92 μmol/ 10mg powder sample, using ICP-AES as elemental analysis method; the amount of Re(I) on Kaolin was determined as 1.95 μmol/ 10mg powder sample by the same analysis technique.

First, the catalytic activity of the "as synthesized" Re-L-NPSiO$_2$ was investigated in DMF solution in presence of the sacrificial electron donor, TEOA and

photosensitizer, $Ru(bpy)_3^{2+}$. The amount of CO generated by Re-L-NPSiO$_2$

during the photocatalytic CO_2 reduction was monitored by GC, under the same

reaction condition as that for Re-L-Kaolin (100 mW/cm^2 visible light irradiation

and same amount of TEOA and $Ru(bpy)_3^{2+}$).
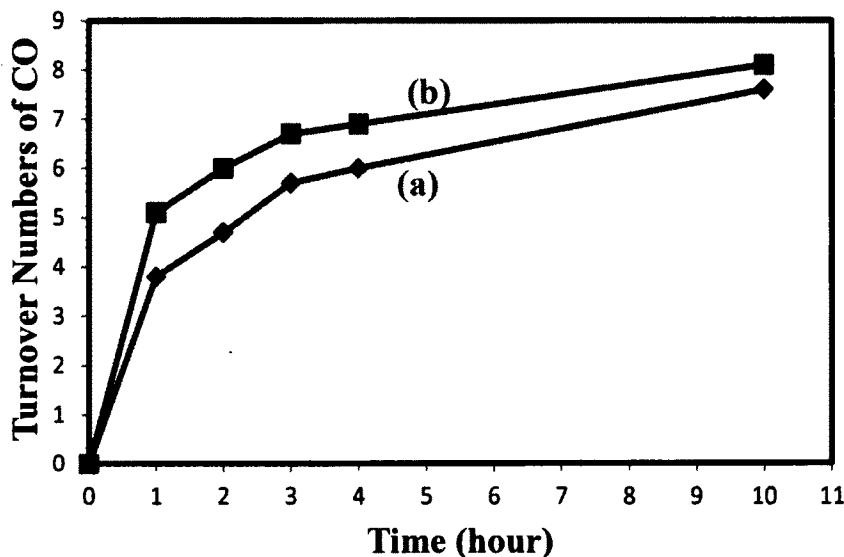
**Figure 5.7 CO TONs of (a) Re-L-Kaolin and (b) Re-L-NPSiO$_2$ at different
reaction time intervals, under the same reaction conditions**

Figure 5.7 illustrates the photocatalytic activities of both the Re-L-Kaolin and Re-

L-NPSiO$_2$ in DMF solution by showing the CO turnover numbers of each catalyst

at different reaction time intervals. The synthesized Re-L- NPSiO$_2$ displays a

slightly better activity than Re-L-Kaolin in a 10-hour CO_2 reduction period.

According to the results, the structural effects of these two solid-state materials

do not bring about a significant difference between the two catalysts in the

photocatalytic reaction.

However, Re-L-Kaolin and Re-L-NPSiO$_2$ exhibited distinct features in the *in situ* solid-state infrared study in the presence of TEOA. To prepare the infrared samples, each catalyst powder was mixed with several drops of TEOA and pressed on a KBr pellet in a three-window photoreaction chamber. After 20 min Ar gas purge, the infrared spectrum of each sample was collected on a Nicolet 6700 FTIR spectrometer with a Harrick Praying Mantis diffuse reflectance accessory. Figure 5.8 shows the FTIR spectra of the Re-L-NPSiO$_2$ + TEOA mixture, the Re-L-SBA-15 + TEOA mixture and the Re-L-Kaolin + TEOA mixture under Ar atmosphere. On the infrared spectrum, the Re-L-NPSiO$_2$ + TEOA mixture only displays 3 strong absorbance peaks at 2020 cm^{-1}, 1917 cm^{-1} and 1894 cm^{-1}, which associate to the surface carbonyl groups of the tricarbonyl Re(I) complex. In the spectra of the Re-L-Kaolin + TEOA and the Re-L-SBA-15 + TEOA, except these 3 peaks, 3 new features in the carbonyl groups absorbance region appear at 1995 cm^{-1}, 1875 cm^{-1} and 1847 cm^{-1}, respectively. The formation mechanism of these new peaks is not clear. One possible reason that accounts for the formation of these new peaks is the meso-pores in SBA-15 and the layers in Kaolin can localize TEOA molecules around the tricarbonyl Re(I) complex to form new species, while the non-porous silica supports can't localize TEOA molecules to interact with the surface immobilized tricarbonyl Re(I) complex. Gibson et al.[77] reported the carbonyl absorbance of a *fac*-Re(I)(CO)$_3$-OH compound, at 2000 cm^{-1}, 1881 cm^{-1} and 1858 cm^{-1}, which are very close to the peak positions (1995 cm^{-1}, 1875 cm^{-1} and 1847 cm^{-1}) found in our infrared spectra. One assumption is the localized TEOA molecules react with residual

water to form OH⁻ and replace the Cl⁻ in the *fac*-tricarbonyl Re(I)-Cl complex, accordingly, a *fac*-tricarbonyl Re(I)-OH species formed to account for the new carbonyl absorbance. The slight difference between the peaks of our Re(I)-OH species and the reported peaks might be due to the amide derivative on the bipyridine ring of our Re(I) material.

It is also noticeable that between the 1700 and 1800 cm^{-1} absorbance region, there are several weak peaks observed in the spectrum of the Re-L-Kaolin + TEOA mixture (Figure 5.8c, not labeled); these peaks might be produced by the surface localized TEOA interact with the surface hydroxyls in Kaolin. Since functionalized silicas do not have spare surface silanol groups to interact with TEOA, these peaks are not seen in the spectra of both Re-L-NPSiO$_2$ + TEOA mixture and Re-L-SBA-15 + TEOA mixture (Figure 5.8a and b).
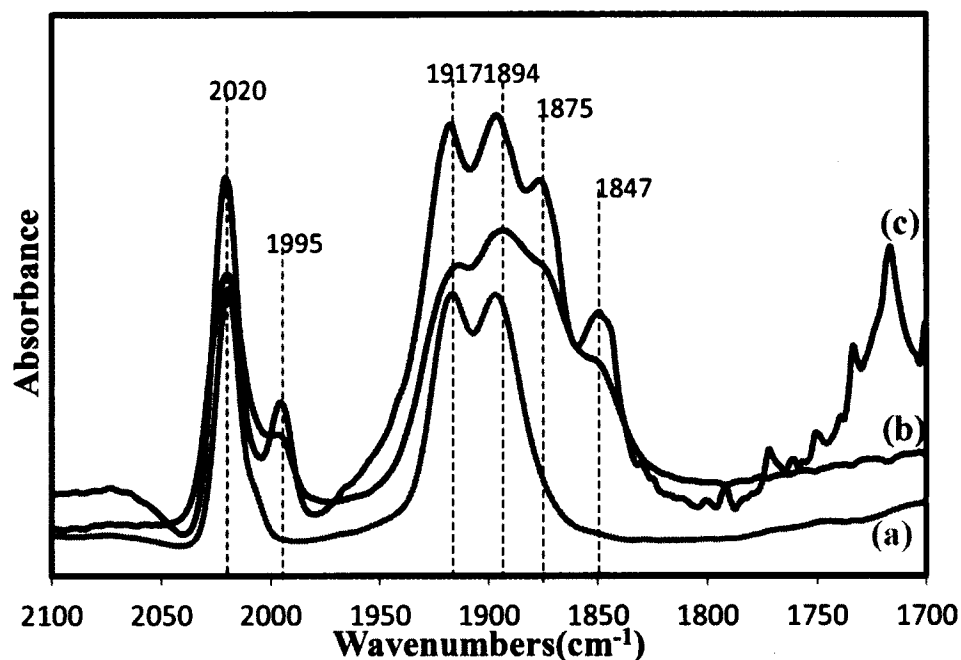
Figure 5.8 FTIR spectra of (a) Re-L- NPSiO₂ + TEOA, (b) Re-L-SBA-15 + TEOA and (c) Re-L-Kaolin + TEOA under Ar atmosphere in dark

Infrared spectrum of the Re-L-NPSiO₂ + TEOA mixture indicates the layered structures of Kaolin have a tremendous effect to the properties of the attached molecular catalyst, especially with the existence of other molecules such as the electron donor, TEOA. To investigate this structural effect during the photocatalytic CO_2 reduction process, a solid-gas interphase photocatalytic CO_2 reduction of the Re-L-Kaolin was studied in a sealed 3-window photoreaction chamber equipped with infrared detector, in the presence of a sacrificial electron donor, TEOA. First, the reaction chamber was purged with CO_2 (99.999%, Airgas) for 20 min in dark and the infrared spectrum of the Re-L-Kaolin + TEOA mixture under CO_2 atmosphere in dark was collected. Next, light irradiation was

introduced to the reaction chamber, using an ozone-free Xe lamp (Newport)

equipped with an AM 1.5 filter. This filter blocks about 50% of the infrared

irradiation from the Xe lamp but does not significantly affect the UV-Vis light

region. After 2 hours UV-Vis irradiation, infrared spectrum of the mixture in the

reaction chamber was also recorded.
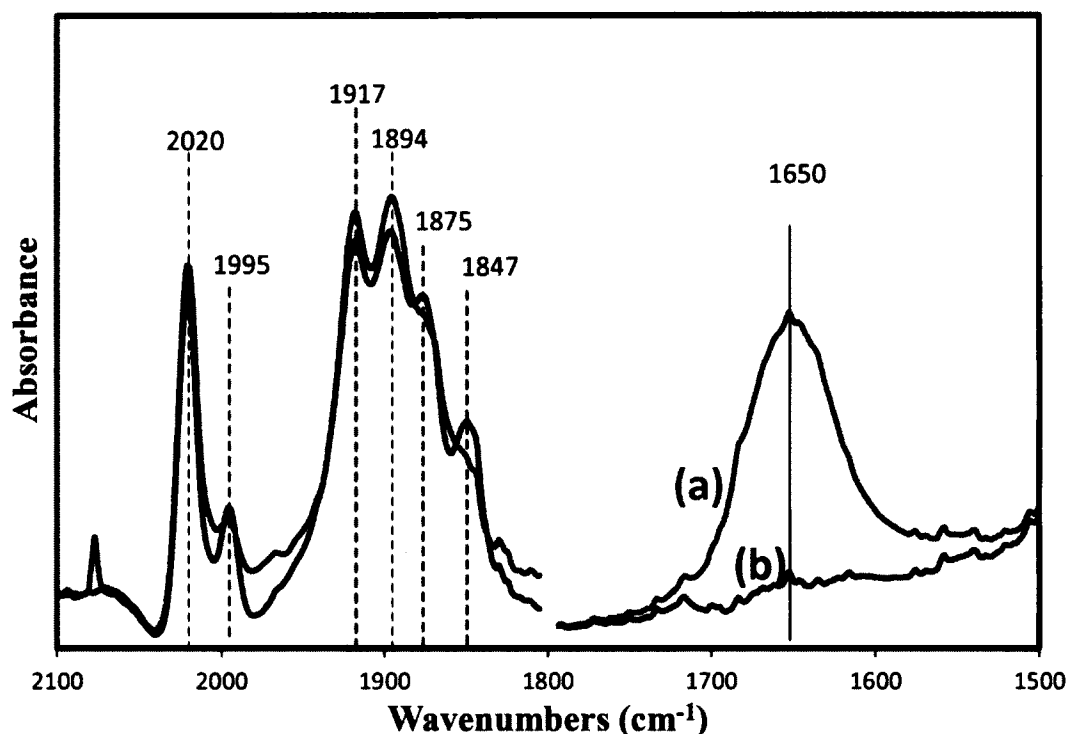
Figure 5.9 FTIR Spectra of (a) Re-L- Kaolin +TEOA purge with CO_2 in dark and (b) Re-L- Kaolin +TEOA purge with Ar in dark

Figure 5.9 shows the infrared spectra of the catalyst and TEOA mixture in dark

under Ar and CO_2 atmosphere. According to the spectra, after purge with CO_2,

carbonyl absorbance peaks do not have significant change although the relative

intensity of these peaks slightly different from that under Ar atmosphere. The strong broad absorbance at 1650 cm^{-1} (Figure 5.9b) is due to the formation of surface absorbed bicarbonate when the mixture exposed to a CO_2 atmosphere, which is the characteristic absorbance of the O–C–O stretching of bicarbonate species.[67]
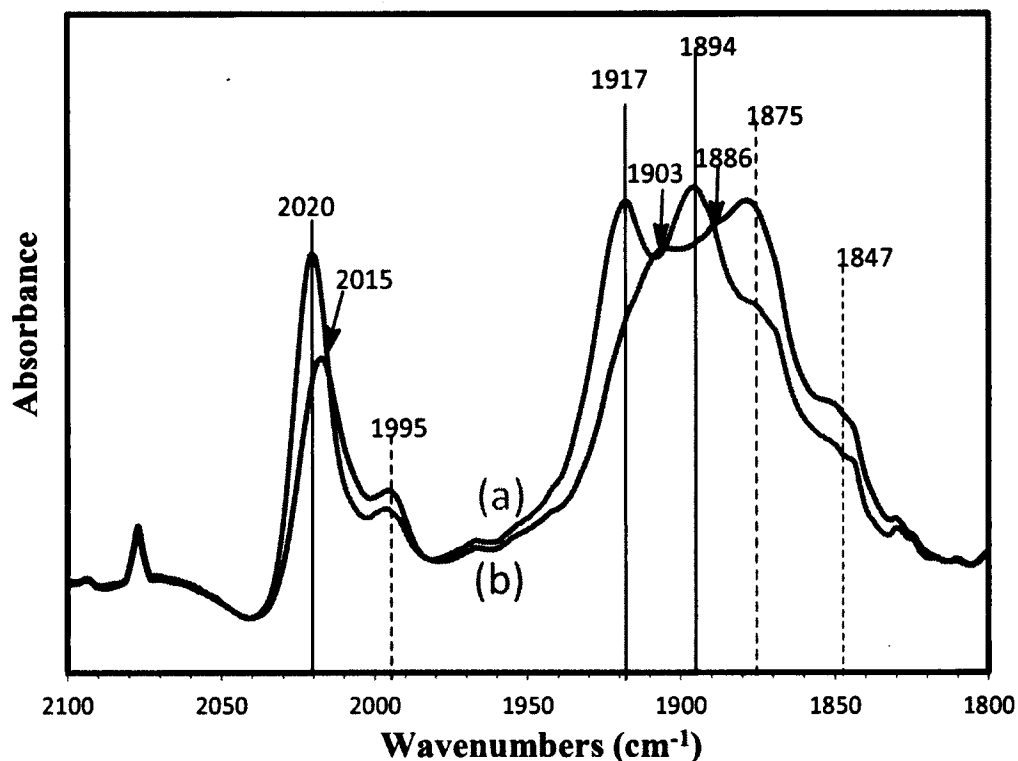
Figure 5.10 FTIR Spectra of (a) Re-L- Kaolin +TEOA purge with CO₂ in dark and (b) Re-L- Kaolin +TEOA purge with CO₂ with Vis-light 2h

After UV-Vis light irradiation, the infrared features of the Re-carbonyl groups have a remarkable change as shown in Figure 5.10. The absorbance peaks at 2020 cm^{-1}, 1917 cm^{-1} and 1894 cm^{-1} shift to lower wavenumbers at 2015 cm^{-1},

1903 cm^{-1} and 1886 cm^{-1}, respectively, with a relative intensity decrease. These shifts are coincident with the results of the *in situ* photocatalytic CO_2 reduction of the Re-L-NPSiO$_2$, reported by Liu et al.[76] The shifts are attributed to the bipyridine-based reduction of Re-L species upon light irradiation. The shifted wavenumbers generated by our surface immobilized catalysts are lower than the reported shift (~20 cm^{-1}) of the primary bipyridine-based reduction produced by a homogeneous Re-bpy[78,79] is due to the existence of an amide (–CONH) group on the bpy ligand in our catalysts.[76] On the contrary, the other set of Re-carbonyl peaks (1995 cm^{-1}, 1875 cm^{-1} and 1847 cm^{-1}) do not have wavenumber shift but get a relative intensity increase after the photoreaction.

In situ infrared spectra were collected by my lab colleague Chao Liu.

5.6 Conclusions

In summary, the photo CO_2 reduction catalyst has been immobilized in the layer structured Kaolin through the covalent amide linkages attached with the inner surface hydroxyl groups in Kaolin. The functionalized Kaolin catalyst exhibits absorbability in visible light range due to the MLCT transition of the tricarbonyl Re (I) complex with derivative amide linkages. In comparison with its homogeneous counterpart, this surface immobilized catalyst also displays an excellent stability during the photocatalytic CO_2 reduction, upon a moderate light

irradiation (100 mW/cm^2). Furthermore, after the photoreaction, the recycled catalyst still retains significant amount of Re (I) compounds in the Kaolin layers, which indicates a good recyclability of this material. Similar to the mesoporous structures in silica, the layered structure of clay material can also effectively protect the Re (I) compound against photochemical decomposition and improve the catalyst stability.

In situ FTIR study reveals some new features of the functionalized Kaolin catalyst, which are not seen in the infrared spectrum of the functionalized non-porous silica material. The formation mechanism of these new features and their properties are not clear, further studies are necessary to investigate the structural effects of Kaolin to the attached molecular catalysts.

LIST OF REFERENCES

1. Song, C. *Catalysis Today* 2006, *115* (1–4), 2-32.

2. Morris, A. J.; Meyer, G. J.; Fujita, E. *Accounts of Chemical Research* 2009, *42* (12), 1983-1994.

3. Hori, H.; Ishitani, O.; Koike, K.; Johnson, F. P. A.; Ibusuki, T. *Energy Conversion and Management* 1995, *36* (6–9), 621-624.

4. Hori, H.; Johnson, F. P. A.; Koike, K.; Ishitani, O.; Ibusuki, T. *Journal of Photochemistry and Photobiology A: Chemistry* 1996, *96* (1–3), 171-174.

5. Arakawa, H.; Aresta, M.; Armor, J. N.; Barteau, M. A.; Beckman, E. J.; Bell, A. T.; Bercaw, J. E.; Creutz, C.; Dinjus, E.; Dixon, D. A.; Domen, K.; DuBois, D. L.; Eckert, J.; Fujita, E.; Gibson, D. H.; Goddard, W. A.; Goodman, D. W.; Keller, J.; Kubas, G. J.; Kung, H. H.; Lyons, J. E.; Manzer, L. E.; Marks, T. J.; Morokuma, K.; Nicholas, K. M.; Periana, R.; Que, L.; Rostrup-Nielson, J.; Sachtler, W. M. H.; Schmidt, L. D.; Sen, A.; Somorjai, G. A.; Stair, P. C.; Stults, B. R.; Tumas, W. *Chemical Reviews* 2001, *101* (4), 953-996.

6. Grills, D. C.; Fujita, E. *The Journal of Physical Chemistry Letters* 2010, *1* (18), 2709-2718.

7. Fan, T.; Chen, X.; Lin, Z. *Chemical Communications* 2012, *48* (88), 10808-10828.

8. Hawecker, J.; Lehn, J.-M.; Ziessel, R. *Journal of the Chemical Society, Chemical Communications* 1983, *0* (9), 536-538.

9. Tamaki, Y.; Watanabe, K.; Koike, K.; Inoue, H.; Morimoto, T.; Ishitani, O. *Faraday Discussions* 2012, *155* (0), 115-127.

10. Crosby, G. A.; Demas, J. N. *Journal of the American Chemical Society* 1971, *93* (12), 2841-2847.

11. Takeda, H.; Ishitani, O. *Coordination Chemistry Reviews* 2010, *254* (3–4), 346-354.

12. Liebau, F. *Microporous and Mesoporous Materials* 2003, *58* (1), 15-72.

13. McCusker, L. B.; Liebau, F.; Engelhardt, G. *Microporous and Mesoporous Materials* 2003, *58* (1), 3-13.

14. Hua, J.; Han, Y. *Chemistry of Materials* 2009, *21* (12), 2344-2348.

15. Song, W.; Grassian, V. H.; Larsen, S. C. *Microporous and Mesoporous Materials* 2006, *88* (1–3), 77-83.

16. Song, W.; Justice, R. E.; Jones, C. A.; Grassian, V. H.; Larsen, S. C. *Langmuir* 2004, *20* (19), 8301-8306.

17. Bell, A. T. *Colloids and Surfaces A: Physicochemical and Engineering Aspects* 1999, *158* (1–2), 221-234.

18. Di Renzo, F.; Cambon, H.; Dutartre, R. *Microporous Materials* 1997, *10* (4–6), 283-286.

19. Beck, J. S.; Vartuli, J. C.; Roth, W. J.; Leonowicz, M. E.; Kresge, C. T.; Schmitt, K. D.; Chu, C. T. W.; Olson, D. H.; Sheppard, E. W. *Journal of the American Chemical Society* 1992, *114* (27), 10834-10843.

20. Zhao, D.; Feng, J.; Huo, Q.; Melosh, N.; Fredrickson, G. H.; Chmelka, B. F.; Stucky, G. D. *Science* 1998, *279* (5350), 548-552.

21. Rahmat, N.; Abdullah, A. Z.; Mohamed, A. R. *American Journal of Applied Sciences 7* (12), 1579-1586.

22. Takeda, H.; Koike, K.; Inoue, H.; Ishitani, O. *Journal of the American Chemical Society* 2008, *130* (6), 2023-2031.

23. Indrakanti, V. P.; Kubicki, J. D.; Schobert, H. H. *Energy & Environmental Science* 2009, *2* (7), 745-758.

24. Jones, C. *Top Catal* 2010, *53* (13-14), 942-952.

25. Takeda, H.; Ohashi, M.; Tani, T.; Ishitani, O.; Inagaki, S. *Inorganic Chemistry* 2010, *49* (10), 4554-4559.

26. White, C. E.; Provis, J. L.; Riley, D. P.; Kearley, G. J.; van Deventer, J. S. J. *The Journal of Physical Chemistry B* 2009, *113* (19), 6756-6765.

27. Anpo, M.; Yamashita, H.; Ichihashi, Y.; Fujii, Y.; Honda, M. *The Journal of Physical Chemistry B* 1997, *101* (14), 2632-2636.

28. Yamashita, H.; Fujii, Y.; Ichihashi, Y.; Zhang, S. G.; Ikeue, K.; Park, D. R.; Koyano, K.; Tatsumi, T.; Anpo, M. *Catalysis Today* 1998, *45* (1–4), 221-227.

29. Stöcker, M. *Microporous and Mesoporous Materials* 2005, *82* (3), 257-292.

30. Nezamzadeh-Ejhieh, A.; Badri, A. *Journal of Electroanalytical Chemistry* 2011, *660* (1), 71-79.

31. Cundy, C. S.; Cox, P. A. *Microporous and Mesoporous Materials* 2005, *82* (1–2), 1-78.

32. Tosheva, L.; Valtchev, V. P. *Chemistry of Materials* 2005, *17* (10), 2494-2513.

33. Cundy, C. S.; Cox, P. A. *Chemical Reviews* 2003, *103* (3), 663-702.

34. Davis, M. E.; Lobo, R. F. *Chemistry of Materials* 1992, *4* (4), 756-768.

35. Cundy, C. S.; Henty, M. S.; Plaisted, R. J. *Zeolites* 1995, *15* (4), 353-372.

36. Dedecek, J.; Balgová, V.; Pashkova, V.; Klein, P.; Wichterlová, B. *Chemistry of Materials* 2012, *24* (16), 3231-3239.

37. Narayanan, S.; Sultana, A.; Krishna, K.; Mériaudeau, P.; Naccache, C. *Catal Lett* 1995, *34* (1-2), 129-138.

38. Song, W.; Grassian, V. H.; Larsen, S. C. *Chemical Communications* 2005, *0* (23), 2951-2953.

39. Flanigen, E. M.; Bennett, J. M.; Grose, R. W.; Cohen, J. P.; Patton, R. L.; Kirchner, R. M.; Smith, J. V. *Nature* 1978, *271* (5645), 512-516.

40. Chang, J.-S.; Hwang, J.-S.; Park, S.-E. *Research on Chemical Intermediates* 2003, *29* (7-9), 921-938.

41. Chen, H.; Kuranari, S.; Akiyama, T.; Zhang, J.; Anpo, M. *Journal of Catalysis* 2008, *257* (1), 215-220.

42. Johansson, E. M.; Ballem, M. A.; Córdoba, J. M.; Odén, M. *Langmuir* 2011, *27* (8), 4994-4999.

43. Melero, J. A.; Stucky, G. D.; van Grieken, R.; Morales, G. *Journal of Materials Chemistry* 2002, *12* (6), 1664-1670.

44. Nguyen, T. P. B.; Lee, J.-W.; Shim, W. G.; Moon, H. *Microporous and Mesoporous Materials* 2008, *110* (2–3), 560-569.

45. Cao, L.; Man, T.; Kruk, M. *Chemistry of Materials* 2009, *21* (6), 1144-1153.

46. Tolbert, S. H. *Nat Mater* 2012, *11* (9), 749-751.

47. Fujita, E. *Coordination Chemistry Reviews* 1999, *185–186* (0), 373-384.

48. Benson, E. E.; Kubiak, C. P.; Sathrum, A. J.; Smieja, J. M. *Chemical Society Reviews* 2009, *38* (1), 89-99.

49. Usubharatana, P.; McMartin, D.; Veawab, A.; Tontiwachwuthikul, P. *Industrial & Engineering Chemistry Research* 2006, *45* (8), 2558-2568.

50. Joshi, U. A.; Palasyuk, A.; Arney, D.; Maggard, P. A. *The Journal of Physical Chemistry Letters* 2010, *1* (18), 2719-2726.

51. Hoffmann, M. R.; Moss, J. A.; Baum, M. M. *Dalton Transactions* 2011, *40* (19), 5151-5158.

52. Copéret, C.; Chabanas, M.; Petroff Saint-Arroman, R.; Basset, J.-M. *Angewandte Chemie International Edition* 2003, *42* (2), 156-181.

53. Li, G.; Sproviero, E. M.; McNamara, W. R.; Snoeberger, R. C.; Crabtree, R. H.; Brudvig, G. W.; Batista, V. S. *The Journal of Physical Chemistry B* 2009, *114* (45), 14214-14222.

54. Jarosz, P.; Du, P.; Schneider, J.; Lee, S.-H.; McCamant, D.; Eisenberg, R. *Inorganic Chemistry* 2009, *48* (20), 9653-9663.

55. Weare, W. W.; Pushkar, Y.; Yachandra, V. K.; Frei, H. *Journal of the American Chemical Society* 2008, *130* (34), 11355-11363.

56. Youngblood, W. J.; Lee, S.-H. A.; Kobayashi, Y.; Hernandez-Pagan, E. A.; Hoertz, P. G.; Moore, T. A.; Moore, A. L.; Gust, D.; Mallouk, T. E. *Journal of the American Chemical Society* 2009, *131* (3), 926-927.

57. Anfuso, C. L.; Snoeberger, R. C.; Ricks, A. M.; Liu, W.; Xiao, D.; Batista, V. S.; Lian, T. *Journal of the American Chemical Society* 2011, *133* (18), 6922-6925.

58. Zhao, C.; Huang, Z.; Rodríguez-Córdoba, W.; Kambara, C. S.; O'Halloran, K. P.; Hardcastle, K. I.; Musaev, D. G.; Lian, T.; Hill, C. L. *Journal of the American Chemical Society* 2011, *133* (50), 20134-20137.

59. Rosenfeld, D. E.; Gengeliczki, Z.; Smith, B. J.; Stack, T. D. P.; Fayer, M. D. *Science* 2011, *334* (6056), 634-639.

60. Wang, C.; Xie, Z.; deKrafft, K. E.; Lin, W. *Journal of the American Chemical Society* 2011, *133* (34), 13445-13454.

61. Lin, W.; Han, H.; Frei, H. *The Journal of Physical Chemistry B* 2004, *108* (47), 18269-18273.

62. Anpo, M.; Thomas, J. M. *Chemical Communications* 2006, *0* (31), 3273-3278.

63. Lin, W.; Frei, H. *Journal of the American Chemical Society* 2005, *127* (6), 1610-1611.

64. Lin, W.; Frei, H. *Comptes Rendus Chimie* 2006, *9* (2), 207-213.

65. Hwang, J.-S.; Chang, J.-S.; Park, S.-E.; Ikeue, K.; Anpo, M. *Top Catal* 2005, *35* (3-4), 311-319.

66. Sung-Suh, H. M.; Kim, D. S.; Lee, C. W.; Park, S.-E. *Applied Organometallic Chemistry* 2000, *14* (12), 826-830.

67. Dubois, K. D.; Petushkov, A.; Garcia Cardona, E.; Larsen, S. C.; Li, G. *The Journal of Physical Chemistry Letters* 2012, *3* (4), 486-492.

68. Chen, H.; Kuranari, S.; Matsuoka, M.; Zhang, J.; Anpo, M. *Catal Lett* 2008, *126* (3-4), 218-223.

69. Corma, A. *Chemical Reviews* 1997, *97* (6), 2373-2420.

70. Vernimmen, J.; Meynen, V.; Cool, P. *Beilstein Journal of Nanotechnology* 2011, *2*, 785-801.

71. Murray, H. H. *Applied Clay Science* 2000, *17* (5–6), 207-221.

72. Frost, R. L. *Clays and Clay Minerals* 1998, *46* (3), 280-289.

73. Frost, R. L.; Vassallo, A. M. *Clays and Clay Minerals* 1996, *44* (5), 635-651.

74. Hu, X. L.; Michaelides, A. *Surf. Sci.* 2008, *602*, 960 - 974.

75. Brigatti, M. F.; Galan, E.; Theng, B. K. G. In *Developments in Clay Science*, Faïza Bergaya, B. K. G. T.; Gerhard, L., Eds. Elsevier: 2006; Vol. Volume 1, pp 19-86.

76. Liu, C.; Dubois, K. D.; Louis, M. E.; Vorushilov, A. S.; Li, G. *ACS Catalysis* 2013, 655-662.

77. Gibson, D. H.; Yin, X.; He, H.; Mashuta, M. S. *Organometallics* 2002, *22* (2), 337-346.

78. Smieja, J. M.; Kubiak, C. P. *Inorganic Chemistry* 2010, *49* (20), 9283-9289.

79. Johnson, F. P. A.; George, M. W.; Hartl, F.; Turner, J. J., Electrocatalytic Reduction of CO_2 *Organometallics* 1996, *15* (15), 3374-3387.